

# **Year-round vertically resolved observations of upper ocean hydrography and biogeochemistry in the Atlantic Water inflow north of Svalbard**

Rebecca McPherson<sup>1</sup>, Normen Lochthofen<sup>1</sup>, Simon F. Reifenberg<sup>1</sup>, Wilken-Jon von Appen<sup>1</sup>, Hongyan Xi<sup>1</sup>

<sup>1</sup>Alfred Wegener Institute, Helmholtz Centre for Polar and Marine Research; Bremerhaven, Germany

## **Abstract**

A novel Subsea Winched Profiling System (SWIPS) was deployed in the Atlantic Water (AW) inflow to the Arctic Ocean north of Svalbard, providing high-resolution, year-round observations of upper ocean hydrography and biogeochemistry. Between July 2022 and July 2023, SWIPS collected 85 vertical profiles from ~125 m to 10 m depth at 4-day intervals, capturing seasonal transitions and fine-scale variability across open water and ice-covered conditions. The autonomous system provides a sustained Eulerian perspective of upper ocean dynamics, resolving the evolving water mass distribution, seasonal stratification, the deepening of the mixed layer in autumn and winter, and the persistent influence of AW beneath a strongly stratified surface layer. SWIPS captured an under-ice phytoplankton bloom in May 2023, occurring under > 80% sea ice concentrations and preceding the onset of Polar Day by more than one week. During peak bloom periods, satellite-derived chlorophyll concentrations underestimated in-situ values by up to an order of magnitude due to persistent subsurface chlorophyll maxima and ice cover. The profiler also detected two episodes of anomalous winter hydrography during which AW reached the surface and disrupted the expected cold, stratified regime. The hydrographic data and satellite sea surface temperature suggest these events were driven by upstream AW advection from Fram Strait and facilitated localized convection to depths exceeding 100 m, reinforcing the role of remote forcing in shaping local upper ocean and ice conditions. By capturing both gradual seasonal evolution and short-lived anomalies, SWIPS provides critical in-situ observations that complement traditional observational methods and improve understanding of ocean–ice–ecosystem interactions under Arctic amplification.

## **1. Introduction**

The Arctic is warming at least twice as fast as the global average (Rantanen et al., 2022) and has lost more than half of its sea ice volume since the early 1980s (Carmack et al. 2015;

Wang et al. 2022). As the ice cover diminishes, the Arctic Ocean absorbs more solar radiation, further enhancing ocean warming and reinforcing the feedback loop termed “Arctic amplification” that influences thermohaline circulation and plays a key role in global climate regulation. While surface-driven melt primarily affects the upper layers of sea ice from above, advective heat from Atlantic Water (AW) contributes to basal ice melt and ice thinning (Liang et al., 2022). Monitoring the transport of AW - the Arctic Ocean’s primary source of heat and salt - and its pathways of horizontal and vertical redistribution is therefore crucial for understanding ice-ocean interactions and broader climate impacts (Carmack et al., 2015; Polyakov et al., 2017). These processes also have far-reaching consequences for upper ocean biogeochemistry, nutrient cycling, and the timing and intensity of phytoplankton blooms — all key indicators of ecological change in the rapidly evolving Arctic system (Soltwedel et al. 2016; von Appen et al. 2021; Salter et al. 2023). To examine how AW affects the upper ocean environment year-round, we use the first full annual dataset from a novel under-ice profiling winch deployed on the Yermak Plateau to investigate seasonal variability in stratification, sea ice cover, and biological signals.

Fram Strait, located between Svalbard and Greenland, is the main gateway for AW entering the Arctic Ocean. Originating in the North Atlantic, AW flows northwards as a topographically steered boundary current through the Nordic Seas to Fram Strait via the West Spitsbergen Current (WSC) (Fig. 1) (Skagseth et al. 2004). The WSC transports heat and nutrients to the central Arctic Ocean, influencing both ocean and sea ice conditions (Aagaard et al. 1987; Torres-Valdés et al. 2013; Polyakov et al. 2017; Docquier et al. 2021). Approximately half of the AW carried by the WSC recirculates westwards across Fram Strait towards Greenland (Quadfasel et al. 1987; Marnela et al. 2013; McPherson et al. 2023; 2024) while the remainder continues into the central Arctic. Long-term observations from a mooring array in the WSC maintained by the Alfred Wegener Institute (AWI) (Fig. 1) identify a sustained warming trend of 0.2°C per decade in the AW inflow between 1997 and 2024 - a total increase of 0.54°C over 27 years (McPherson et al. 2025 - this issue).

North of Svalbard, the WSC further splits into three branches which are guided by the bathymetry of the Yermak Plateau (~ 700m depth) (Fig. 1): 1. the shallow Svalbard Branch (SB) which follows the 400–500 m isobaths eastward along the Svalbard continental slope (Muench et al. 1992; Cokelet et al. 2008); 2. the deeper Yermak Branch (YB) which follows the 1,500 m isobath along the western slope (Manley, et al. 1992); and. 3. the Yermak Pass Branch (YPB) which crosses the plateau along the 700–800 m isobaths and is the dominant AW pathway in winter (Koenig et al. 2017; Menze et al. 2019). Model estimates suggest the YPB carries over 50% of the AW inflow ( $1.2 \pm 0.8$  Sv), while the SB transports ~25% ( $0.6 \pm$

0.3 Sv), with a further contribution from the YB ( $0.5 \pm 0.4$  Sv) and other recirculations (Athanase et al., 2021). The extent of the AW modification - cooling and freshening - depends on the pathway taken over or around the plateau (Fer et al. 2010).

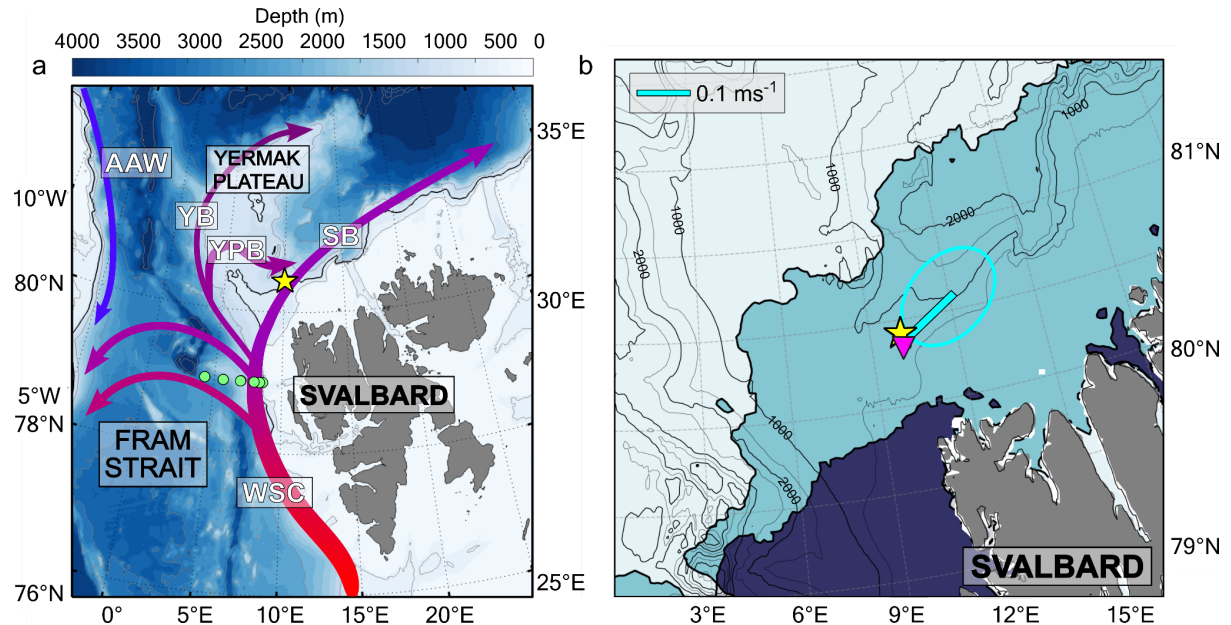


**Figure 1: Map of the Atlantic Water (AW) circulation in Fram Strait and the Yermak Plateau.** (a) The location of the moorings on the Yermak Plateau (yellow star), and the mooring array across the West Spitsbergen Current (WSC) in the eastern Hausgarten region (green circles). The WSC carries warm AW northwards, splitting into the eastward flowing Svalbard Branch (SB; southern route across the Yermak Plateau), Yermak Branch (YB; northern route around the Yermak Plateau), and Yermak Plateau Branch (YPB; main route of AW across the Yermak Plateau), as well as recirculating in Fram Strait. AW entering the Arctic Ocean is modified there and exported through Fram Strait as Arctic Atlantic Water (AAW) many years later. (b) Map of study region with SWIPS winch mooring (Y2-1; yellow star) and neighbouring mooring (Y1-1; pink triangle) locations. The mean (cyan line) and standard deviation (ellipse) of velocity at 55 m at Y1-1 is shown. Two realisations of ice edges represent retreated (white, 15 September 2022) and advanced (pale blue, 15 May 2023) ice cover. The dark blue is open ocean.

The sea ice cover on the Yermak Plateau and northern Fram Strait includes the marginal ice zone (MIZ) - a dynamic transition region between consolidated ice pack and the open ocean that can span tens to hundreds of kilometers (Strong and Rigor 2013; Dumont 2022). The MIZ is characterized by exchanges of energy and heat between ocean, sea ice and atmosphere, strong lateral buoyancy gradients, and enhanced primary production (Johannessen et al. 1987; von Appen et al. 2018; Hofmann et al. 2024). Partial sea ice cover

(< 100%) and cold atmospheric conditions in the MIZ can lead to cooling of the ocean surface and drive localized convection that transports the heat stored in deeper water to the surface where it is lost to the atmosphere. This convection plays a key role in redistributing heat and modifying water mass properties, especially during winter when buoyancy loss at the surface is strongest. The extent of winter convection is strongly regulated by both ice cover - which limits the heat exchange between ocean and atmosphere and suppresses vertical mixing (Fu and Myers, 2024) - and atmospheric forcing, such as strong winds and persistent cold temperatures, which intensifies surface turbulence and promotes deeper mixing (Timmermans and Marshall 2020).

Interactions between sea ice, light availability, and water column stratification in the MIZ strongly shape phytoplankton bloom progression and broader ecosystem responses to Arctic amplification. The formation and recession of sea ice is the most influential environmental variable impacting Arctic marine ecosystems (Laidre et al., 2008), and changes in the ice cover affect bloom dynamics and impact primary production (Ardyna and Arrigo, 2020). To understand the impact of climate change on marine ecosystems, biota must be monitored over the same time scales at which the hydrographic variability occurs. While satellite observations can detect open-water blooms due to their large spatial extent and surface expression, they can miss deep chlorophyll maxima, particularly in stratified conditions, and under-ice blooms (Matthes et al., 2023; Villareal et al., 2011). These limitations underscore the need for high-resolution, vertically resolved time series to capture the timing, magnitude, and structure of primary production — particularly in transitional or ice-covered regimes.

Despite the importance of resolving upper-ocean structure and biological variability in the AW inflow north of Svalbard, in-situ observational gaps remain. Traditional ship-based hydrographic surveys are often limited to the ice-free months (July - October) (e.g., Lundsgaard et al. 2021) and provide a single-point ‘snapshot’. Moorings offer longer timeseries but typically sample at fixed discrete depths (though some acoustic instruments, e.g., ADCPs, can sample distances of over 100 m from their moored position) and often lack the vertical resolution needed to resolve fine-scale stratification or transient features like under-ice blooms and deep chlorophyll maxima. Recent work highlights the importance of near-surface observations to investigate the effects of meltwater-driven stratification on upper ocean mixing (Randelhoff et al. 2017; Fer et al. 2022; Reifenberg et al. 2025).

To capture the evolving vertical structure of the upper ocean, a range of autonomous profiling systems have been developed. Argo floats (Roemmich et al., 2019) and ice-tethered profilers (ITPs; Timmermans et al. 2008) provide semi-Lagrangian observations

in the open ocean and pack ice, respectively, but are largely absent from the MIZ. Other semi-Lagrangian systems like SUCA (Stevens et al. 2005; McPherson et al. 2019) and gliders provide mobile measurements but lack repeated vertical sampling at a fixed location. Tethered profilers such as the McLane Moored Profiler (MMP; Morrison et al. 2000) and Wirewalker (Smith et al., 2011) offer vertically resolved time series but their ability to sample near the surface is limited by buoyancy. Winch-based profilers address this limitation, offering high-resolution, vertically resolved Eulerian observations in the upper ocean (Prien and Schulz-Bull 2016; Hamilton et al. 2013). Early systems like the Icycler (Fowler et al. 2004) and its successor SeaCycler (Send et al., 2013) were developed specifically for use under sea ice. More recently, the Subsurface Winched Profiling System (SWIPS), developed at AWI (Lochthofen et al., 2021), has advanced this capability by enabling repeated high-resolution profiles from 150 m to the ocean surface, with real-time pressure monitoring to protect the system in rough or ice-covered conditions. SWIPS therefore fills a critical gap in Arctic observational capabilities by bridging open-ocean and ice-covered environments.

This study presents the first full-year deployment of a SWIPS mooring in the Svalbard Branch of the AW inflow to the Central Arctic Ocean, approximately 200 km downstream of the WSC mooring array in the main HAUSGARTEN area (McPherson et al. 2025 - this issue). The system operated from summer 2022 to summer 2023 and collected high-resolution, vertically resolved hydrographic and biogeochemical profiles to resolve seasonal variability in upper-ocean structure and phytoplankton dynamics. Specifically, we examine how stratification and mixing evolve throughout the year, and how these processes influence the timing of bloom development across the MIZ. We present and analyse the novel observations during key seasonal events, such as the spring bloom and winter convection, and evaluate the advantages of Eulerian profiling compared to traditional observational approaches that lack temporal resolution (e.g., ship-based surveys), vertical structure (e.g., moored instruments), or sub-surface coverage (e.g., remote sensing). Together, the results demonstrate how SWIPS provides new insight into upper-ocean variability and ice-ocean-biological interactions in a rapidly changing Arctic system.

## 2. Data and Methods

### 2.1. SWIPS Winch System

An oceanographic mooring (Y2-1) equipped with the Subsea Winched Profiling System (SWIPS, Sn: 001) was deployed from 18 July 2022 with RV Polarstern during cruise PS131 and recovered on 23 June 2023 during cruise PS137. The mooring was located at 80° 25.00'

N, 10° 3.65' E on the Yermak Plateau at 693 m depth within the Svalbard branch of the Atlantic Water inflow to the Arctic Ocean (Fig. 1). The mooring was deployed in ice-free conditions, approximately 50 km from the ice edge, and was recovered under moderate sea ice cover (approx. 60% SIC) (Fig. 3c).

The SWIPS winch system, developed at AWI and comprehensively described in Lochthofen et al. (2021), is capable of operating at depths of up to 200 m; in this study, it was installed 125 m below the surface to autonomously capture high-resolution hydrographic and biogeochemical profiles. It consisted of two components: the winch unit which controlled the vertical profiling at pre-programmed intervals, and the profiling unit which housed oceanographic sensors (Fig. 2a,b), forming the upper part of the mooring. Both units were connected via an electromechanical cable that transmits data and power while supporting the mechanical load. The profiling interval was set to 4 days (96 hours) with data acquisition starting on 22 July 2022, 12:00 UTC. To account for anticipated sea-ice coverage, the profiling depth was limited to 10 metres, though the final depth was typically ~9.5 m due to a slight delay in winch response. Over the 343 deployment days, a total of 85 profiles were recorded (Supplementary Figure 1). The profiling speed was approx.  $10 \text{ m min}^{-1}$  which, with a 1-Hz sampling frequency of the attached instruments, resulted in a vertical resolution of 0.1 - 0.15 m, though the ascending speed varied slightly due to the changing drum diameters during unwinding at a constant angular speed.

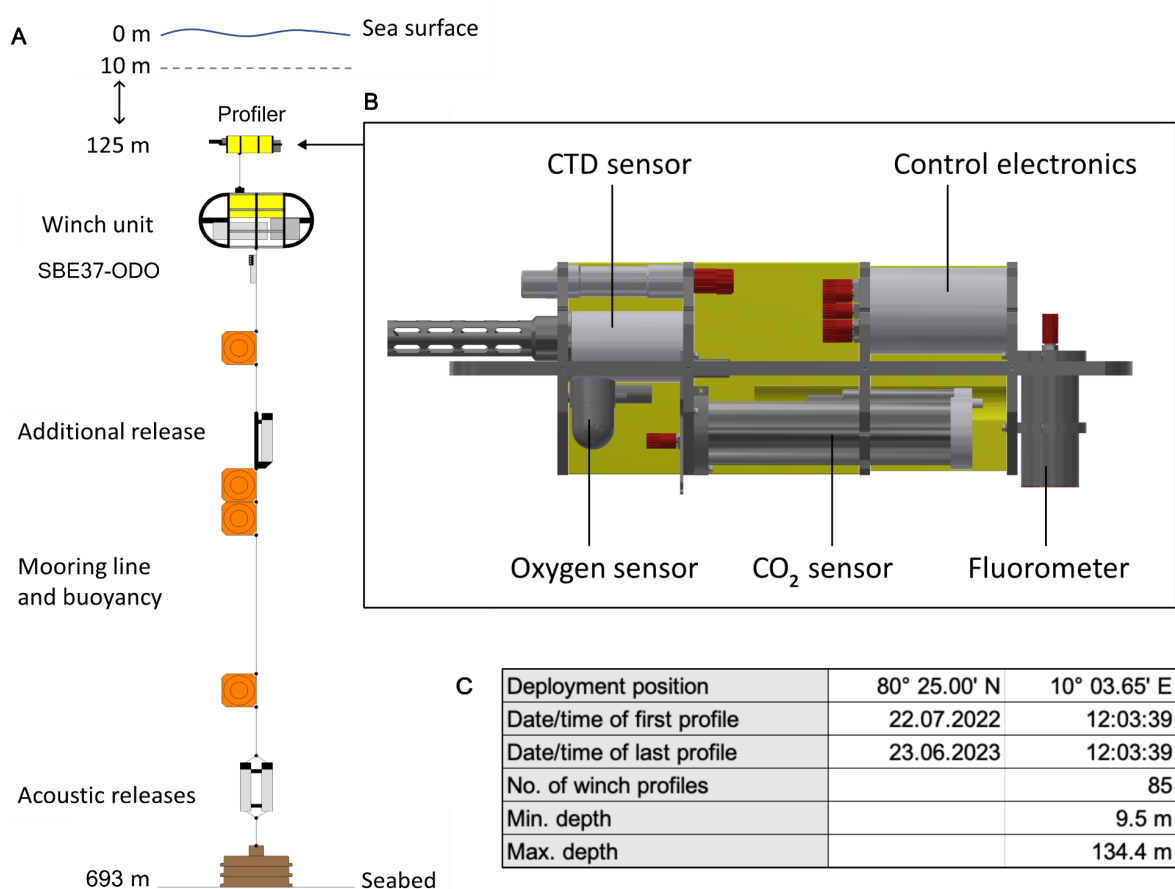


**Figure 2: Schematic of winch and profiler.** a) Schematic of the Y2-1 mooring deployed at 693 m on the Yermak Plateau (Fig. 1), showing the vertical distribution of the winch and profiler system, the acoustic releases and flotation, (b) a simplified section (without the cabling) through the profiling unit with the mounted instrumentation labelled and (c) an overview table of the Y2-1 mooring.

The profiling unit was equipped with a range of sensors, all sampling at 1 Hz. A CTD sensor (Sea-Bird SBE 52-MP) measured temperature, conductivity and pressure. The pressure data was used to determine the position of the profiler in the water column thus also controlling the winch operation. The configuration also included an oxygen sensor (Sea-Bird SBE 63), a fluorometer (Wet Labs ECO Triplet-w) for measuring chlorophyll-a (Chl-a), CDOM fluorescence, and backscatter, as well as a sensor for determining dissolved carbon dioxide (CONTROS HydroC CO<sub>2</sub>). Additional sensors, such as an in-house developed particle camera, can also be integrated on the profiling unit.

A separate acoustic releaser was positioned below the SWIPS, above the main buoyancy, in addition to the standard pair of acoustic releasers at the mooring base (Fig. 2a). This divided the mooring into two separate sections, allowing independent recovery of the SWIPS winch

system separate to the rest of the mooring line and flotation below. By releasing the winch first, it protects the system both from possible entanglements and damage from below, and enables a faster recovery in the case of sea-ice. During PS137 (23 July 2023), a large ice floe drifted over the mooring position, preventing the recovery of the lower mooring section. This was later recovered during PS143\_2 on 24 July 2024.

The hydrographic and biogeochemical data were averaged over 0.1 m intervals from the bottom to the top of each profile. Small data gaps (< 0.2 m), particularly from the biogeochemical sensors, were vertically interpolated and those profiles marked with a red triangle (e.g. in Fig. 8a). Larger data gaps were left unmodified.

## 2.2 Complementary mooring data from an adjacent location

A second oceanographic mooring (Y1-1) was deployed at 80° 24,08'N, 10° 03,66'E, approximately 1.5 km southeast of Y2-1 mooring with the SWIPS profiler (Fig. 1b). The water depth was 689 m. The mooring was equipped with temperature loggers (SBE56), conductivity-temperature-depth (CTD) loggers (SBE37), and two upward-facing Acoustic Doppler Current Profilers (ADCP, RDI WH 300 kHz; RDI LR 75 kHz) with vertical resolutions of 2 m and 8 m, respectively (Table 1).

Depth (m)	Instrument	Start Date	Start Time	Interval (min)
19	SBE37 SMP-ODO	17.07.22	00:00	60
24	SBE56	01.07.22	00:00	0.5
29	SBE56	01.07.22	00:00	0.5
39	SBE37 SMP-ODO	17.07.22	00:00	60
50	SBE56	01.07.22	00:00	0.5
51	ADCP (WH)	18.07.22	08:00	15
60	SBE56	01.07.22	00:00	0.5
70	SBE37-SMP	17.07.22	00:00	10
80	SBE56	01.07.22	00:00	0.5
110	SBE37-SMP	17.07.22	00:00	10
150	SBE56	01.07.22	00:00	0.5
200	SBE56	01.07.22	00:00	0.5
250	SBE37-SMP	17.07.22	00:00	10
301	ADCP (LR)	18.07.22	08:00	30
402	SBE56	01.07.22	00:00	0.5
496	SBE56	01.07.22	00:00	0.5
681	SBE37-SMP	17.07.22	00:00	10

**Table 1. Overview of Y1-1 mooring.** Summary of the instruments on the Y1-1 mooring, with the depth of their deployment, start date and time, and sampling interval. SBE37s measure conductivity, temperature and pressure and SBE37-ODO also measure oxygen; SBE56s measure temperature; and ADCPs (acoustic Doppler current profilers) measure current

velocities. A 300 kHz Workhorse (WH) as well as a 75 kHz Long-ranger (LR) ADCP were deployed.

For analysis, all sensor data were interpolated to a common hourly time grid. The ocean current profiles of the lower ADCP are used in this analysis and the upper (WH) ADCP data are excluded due to ongoing quality measures related to compass issues. Given that the profiling interval of SWIPS exceeded dominant tidal periods, the ADCP velocity record was de-tided using a 40-hr Butterworth filter, removing tidal imprints. However, it is important to note that tides play a significant role in velocity variations and mixing on the Yermak Plateau within the YPB, where mean speeds of  $0.1 \text{ m s}^{-1} \pm 0.05 \text{ m s}^{-1}$  have been recorded (Koenig et al. 2017). Daily mean velocities and hydrographic properties were then computed for further analysis.

## 2.3. Quantities derived from the SWIPS profiles

### 2.3.1. Water mass classification

The different water masses identified in our data set are outlined in Table 2 and shown in both the vertical (Figure 4e) and T/S plane (Fig. 6). There are four water types, following the classification by Rudels et al. (2000) and Meyer et al. (2017).

**Table 2: Water mass definitions.** Following the classification by Rudels et al. (2000) and Meyer et al. (2017), where  $T$  is the potential temperature and  $\sigma$  is the potential density.

Water Mass	Definition
Atlantic Water (AW)	$T \geq 2^\circ\text{C}$ , $27.7 \leq \sigma < 27.97$
Modified Atlantic Water (MAW)	$T < 2^\circ\text{C}$ , $27.7 \leq \sigma < 27.97$
Polar Surface Water (PSW)	$T < 0^\circ\text{C}$ , $\sigma < 27.7$
Warm Polar Surface Water (PSWw)	$T \geq 0^\circ\text{C}$ , $\sigma < 27.7$

### 2.3.2. Stratification

Based on the temperature and salinity measurements for each profile, the buoyancy frequency is calculated as  $N^2 = \sqrt{-\frac{g}{\rho_0} \frac{\Delta\rho}{\Delta z}}$  where  $g$  is the acceleration due to gravity,  $\Delta\rho$  is the potential density difference over the vertical distance of  $\Delta z = 0.1 \text{ m}$ , and  $\rho_0$  is the

average density. For calculation, we first low-pass filtered the vertical density distribution with a 2 m cutoff.

### 2.3.3. Mixed layer depth (MLD)

There are multiple approaches to estimating the mixed layer depth (MLD) from hydrographic data, as well reviewed in Peralta-Ferriz & Woodgate (2015). In this study, the MLD is defined at each time step as the depth at which the potential density difference ( $\Delta\rho$ ) between the uppermost (typically 9.5 m) temperature/salinity measurements exceeds  $0.1 \text{ kg m}^{-3}$ . This density-based approach is used instead of the temperature-only criterion because of the strong salinity influence on density in cold Arctic waters. We note that this method does not account for variability above  $\sim 10$  m depth so the MLD may be overestimated in cases of strong near-surface stratification.

To assess the sensitivity of the MLD results to this choice, we compare our  $\Delta\rho = 0.1 \text{ kg m}^{-3}$  threshold method with three alternatives commonly used in the Arctic Ocean. 1. A smaller threshold criteria of  $0.05 \text{ kg m}^{-3}$  (von Appen et al. 2021); 2. The depth of maximum stratification ( $N^2$ ) (Renner et al. 2023); 3. A relative-density method, where the MLD is the deepest level where the potential density is within 20% of the density difference between the shallowest and the deepest density measurement (Shaw et al., 2009). All four methods generally agree when there is a sharp pycnocline and the gradient of potential density changes sharply (Supplementary Figure 2a), while there is a wider range of estimates for more weakly stratified profiles (Supplementary Figure 2b). Almost 75% of the alternative MLD estimates fall within 5 m of the chosen  $\Delta\rho = 0.1 \text{ kg m}^{-3}$  threshold method for all profiles. Generally, the smaller  $\Delta\rho = 0.05 \text{ kg m}^{-3}$  threshold tends to underestimate MLD in profiles with less steep density gradients, while the stratification-based method tends to overestimate MLD as it tends to capture the onset of stratification rather than the full mixed layer depth (Jackson et al. 2012). Despite these differences, the temporal evolution of the MLDs is generally consistent across methods (not shown).

The chosen threshold criteria of  $\Delta\rho = 0.1 \text{ kg m}^{-3}$  falls within the commonly used range of density thresholds used in the Arctic Ocean ( $\Delta\rho = 0.03 - 0.3 \text{ kg m}^{-3}$ ; Jackson et al. 2012; Steele et al. 2011) and provides a good balance between resolving strong and weak stratification. Therefore, while alternative thresholds yield slightly different values, they would likely provide similar results to the analysis presented here.

#### 2.3.4. Apparent oxygen utilization (AOU)

Dissolved oxygen was measured by the SBE63 optical oxygen sensor mounted on the profiler. To verify sensor performance and correct for any offset, oxygen concentrations from the profiler at ~130 m depth were compared with those from a co-located SBE37-ODO sensor positioned 3 m below the winch (Fig. 2a). This reference sensor showed consistent temperature and salinity values with the profiler, confirming that both sensors generally sampled the same water mass. A mean offset of 1.7  $\mu\text{mol l}^{-1}$  was found between the two oxygen sensors at depth, and this value was applied as a correction to the profiler oxygen data. Apparent Oxygen Utilization (AOU) was calculated as the difference between the atmospherically equilibrated oxygen concentration and the corrected oxygen concentration. Applying the 1.7  $\mu\text{mol l}^{-1}$  correction to oxygen resulted in an ~8  $\mu\text{mol l}^{-1}$  downward adjustment to AOU values using the period between March - April 2023 as a time of expected local convection in the PW when AOU is anticipated to be approximately zero (i.e., 100% oxygen concentration).

#### 2.3.5. Ekman Depth

To further interpret variations in MLD, the theoretical Ekman depth in the absence of ice ( $D_E$ ) is calculated as an indicator for how deep wind-driven mixing could reach, since in its simplest form,  $D_E$  is proportional to wind speed (Pond & Pickard, 1983) :

$$D_E = \frac{\pi \rho_a c_d}{\sqrt{2} \rho_w \Omega \alpha} \frac{1}{\sqrt{\sin \theta}} W$$

with  $\rho_a$  = density of air ( $1.3 \text{ gm}^{-3}$ ),  $c_d$  = drag coefficient (taken as  $1.4 \times 10^{-3}$ ),  $\rho_w$  = density of water ( $1026 \text{ gm}^{-3}$ ),  $\Omega$  = rotation rate of the Earth,  $\theta$  = latitude ( $80.4^\circ\text{N}$ ),  $\alpha$  = empirical constant (0.0127) and  $W$  = wind speed (see e.g., Peralta-Ferriz and Woodgate 2015; Renner et al. 2023). We note that this relationship may be strongly altered by sea ice, especially modulated by differences in sea ice concentration, thickness, and floe shape/size. While  $D_E$  does not directly equate to the actual wind-driven mixing depth, it is a more comprehensive parameter for relating to MLD than wind speed alone, particularly in ice-free conditions (Cole et al., 2017).

#### 2.3.6. MLD heat content and flux

The potential ocean heat content of the mixed layer (i.e., the ocean heat available in the MLD to melt ice) is calculated as  $Q = \rho c \Delta T$  where  $\rho$  is the density of seawater (taken at  $1026 \text{ kgm}^{-3}$ ),  $c$  is the specific heat capacity of seawater, and  $\Delta T$  is the temperature above the freezing point, interpolated to the surface.  $Q$  is then integrated over the depth of the mixed

layer. The heat flux is estimated by dividing the MLD-integrated heat content over 4 days to align with the profiling frequency of the SWIPS. It is assumed that the difference in MLD-integrated heat content between consecutive profiles 4 days apart is solely explained by ocean-to-atmosphere heat flux. This calculation assumes a locally closed vertical heat budget, i.e., that changes in MLD heat content are driven solely by vertical fluxes and do not include lateral (advection) heat transport. This simplification is commonly applied in Arctic heat budget estimates and is reasonable for assessing first-order surface fluxes but may introduce uncertainty during periods of strong advection.

How much ice this MLD-integrated heat flux could melt, assuming all the heat went into directly melting ice and not accounting for heat loss to the atmosphere, is the heat flux divided by the energy required to melt a unit volume of sea ice,  $E = L\rho_{ice}$ , where  $L$  is the latent heat of fusion ( $333.4 \text{ kJ kg}^{-1}$ ) and  $\rho_{ice}$  is the typical density of first-year sea ice ( $917 \text{ kg m}^{-3}$ ).

## 2.4. Satellite-Based Surface Chlorophyll Concentrations

Surface chlorophyll-a (Chl-a) concentration derived from satellite observations were obtained from the ocean colour products available on the Copernicus Marine Service Data Store (<https://data.marine.copernicus.eu>). Three Chl-a products were considered: GlobColour gap-free, OCCCI and CHL-Arc data sets, each derived using different ocean color algorithms. The GlobColour gap-free Chl-a product was selected for comparison with the SWIPS profiler data due its better coverage over the deployment period. The CHL-Arc dataset, which is specifically tuned to Arctic water types, had limited matchup data points due to clouds or ice conditions, preventing its inclusion in this study. A full in-situ and satellite Chl-a comparison is provided in Supplementary Figure 5.

Daily Chl-a data with 4-km resolution were extracted at the mooring location between July 2022 and July 2023, representing an integrated signal from the upper ocean layer (approximately the first optical depth). The matchup criteria follows the EUMETSAT protocol for ocean color data validation (Xi et al. 2020), using  $3 \times 3$  pixels ( $\sim 12 \times 12 \text{ km}$ ) area centred on the mooring. To improve data coverage, a regional time series of Chl-a between April 2022 to September 2023 is also generated using the mean Chl-a over  $100 \times 100 \text{ km}$  macro-pixels around the mooring location, as ocean colour products are heavily weather dependent. Additionally, monthly Chl-a maps were produced for the eastern Fram Strait ( $78^\circ\text{N}$  to  $81^\circ\text{N}$ ,  $5^\circ\text{E}$  to  $15^\circ\text{E}$ ) to visualise phytoplankton bloom development over time.

## 2.5. Satellite Sea Surface Temperature Data

Sea surface temperature (SST) is taken from the high-resolution blended product of in-situ and satellite data provided by the GHRSST project from both infrared and microwave radiometers for the years 2022 - 2023. The data are mapped onto a  $0.05^\circ \times 0.05^\circ$  (6 km x 6 km) global grid at a daily resolution.

## 2.6. Atmospheric reanalysis

ERA5 reanalysis at the surface is globally gridded ( $0.25^\circ \times 0.25^\circ$ ), which is 30 km by 6 km in the area of interest, and at 12-hourly resolution. Air temperature at 2 m height and wind speed at 10 m height are extracted for the mooring position by nearest-neighbor interpolation in space and time. While the 12-hour resolution does not capture sub-daily atmospheric processes near the MIZ, it is consistent with the temporal resolution of the SWIPS profiles (4-day interval), and appropriate for the seasonal-scale variability investigated here.

## 2.7. Sea ice concentration and thickness

Sea ice concentration and thickness is obtained from the AWI AMSR2 ice concentration product v1.10, which has a 3 km spatial resolution and is generated twice daily. Since satellite-derived sea ice thickness is only reliable during the cold seasons, the processing is limited to between mid-October to mid-April. Thus the sea ice concentration data for the rest of the year is supplemented with ERA5 reanalysis data, which provides hourly resolution estimates (Hersbach et al., 2023), from which daily means are calculated. When the two products overlap, they exhibit a strong correlation ( $R = 0.97$ ,  $P < 0.01$ ). ERA5 sea ice data is globally gridded ( $0.25^\circ \times 0.25^\circ$ ) and incorporates two sea ice products: the OSI SAF operational sea ice product (part of the UK MetOffice Operational Sea Surface Temperature), and Sea Ice Analysis (OSTIA). Daily sea ice drift data were also obtained primarily from the OSI SAF product, which has a spatial resolution of 60 km, and used to characterize regional ice movement near the mooring.

# 3. Results

## 3.1. Ice cover and environmental forcing at the mooring location

We present the environmental conditions at the mooring location, focusing on the wind speed, air temperature and ice cover as they relate to processes that influence upper-ocean properties and phytoplankton dynamics.

The mooring location remained ice-free from mid-July to mid-October 2022 after which sea ice concentration rapidly increased, reaching a local maximum of 80% coverage and a thickness of 1.8m by late December (Fig. 3c). In February 2023, a sharp decline in sea ice concentration (SIC) resulted in a brief, three-week period of ice-free conditions (< 20% SIC). Following this anomaly, ice coverage re-established and reached a maximum of nearly 100% by late March 2023 with a thickness of ~2 m. SIC persisted at > 75% coverage through to mid-June after which there was a rapid decline associated with the onset of melting, though the mooring location remained ice-covered until the recovery in July 2023. Over the 11-month deployment, the mooring was under ice for approximately 8 months.

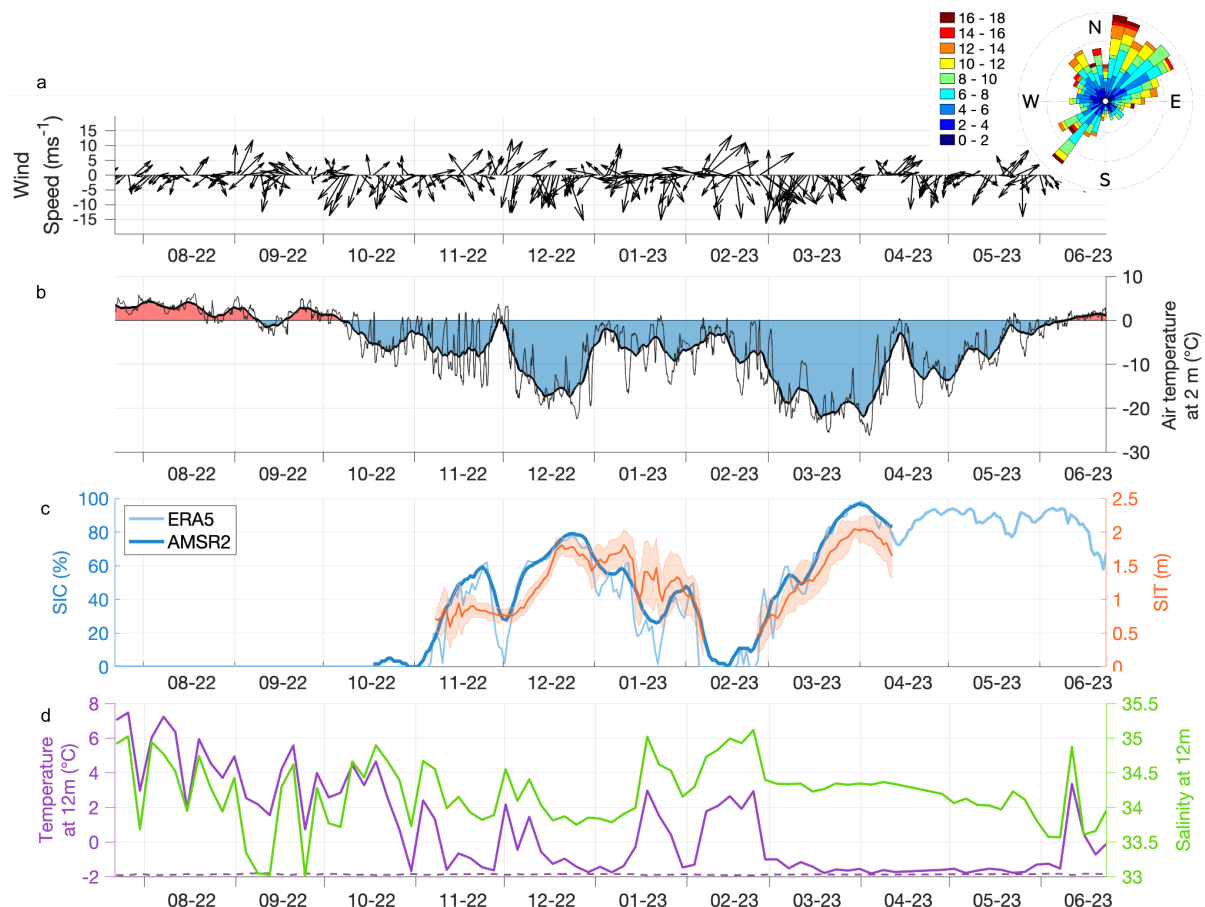


**Figure 3.** Timeseries of environmental background conditions, showing (a) daily 10 m wind direction and wind rose ( $\text{ms}^{-1}$ ), (b) 2 m air temperature (daily and 7-day filtered), (c) sea ice concentration from ERA5 (light blue) and AMSR2 (dark blue), and sea ice thickness (orange), and (d) near-surface (12 m depth) ocean temperature (purple), salinity (green), as well as the freezing point temperature (purple, dashed) calculated from the 12 m salinity, as measured by the winch from July 2022 to June 2023.

Wind conditions were predominantly towards the south-west, with the strongest winds (up to  $15 \text{ ms}^{-1}$ ) occurring between December and March (Fig. 3a). Periods of sustained high wind

speeds from the north during winter corresponded with colder air temperatures which reached -20°C (Fig. 3b). However, brief warming episodes in late November and throughout January reached nearly 0°C and occurred during southerly wind events (Fig. 3a). These southerly winds and warming air temperatures also coincided with decreases in sea ice concentration and thickness (Fig. 3c), suggesting wind-driven northward sea ice drift. Air temperatures began to rise in April and surpassed 0°C by mid-June (Fig. 3b), coinciding with the reduction in SIC (Fig. 3c).

### 3.2. Hydrographic structure and variability

The upper water column was dominated by persistent year-round warm, saline Atlantic Water (AW) between the depths of 40 m and 125 m (see water mass definitions in Table 2) (Fig. 4a,b,e). Between July and mid-October, warm Polar Surface Water (wPSW) generally overlaid the AW layer though colder (< 2°C) Modified Atlantic Water (MAW) intrusions appeared intermittently at mid-depths (40 - 100m), lasting 8 - 12 days (2 - 3 profiles). Notably, three profiles in early September captured subsurface parcels of Polar Surface Water (PSW) between 40 - 70 m, indicating episodic cold-water intrusions. Near-surface temperatures exceeded 7°C in the upper 20 m (Fig. 4a), marking a seasonal high that allowed for the development of a strong thermocline. This intense surface warming led to pronounced near-surface stratification ( $N^2 > 10^{-3} \text{ s}^{-1}$ ) which persisted until early October (Fig. 4d) and confined the mixed layer to relatively shallow depths (20–30 m), though the true MLD may have been even shallower given the detection limit of 10 m (Fig. 4c).

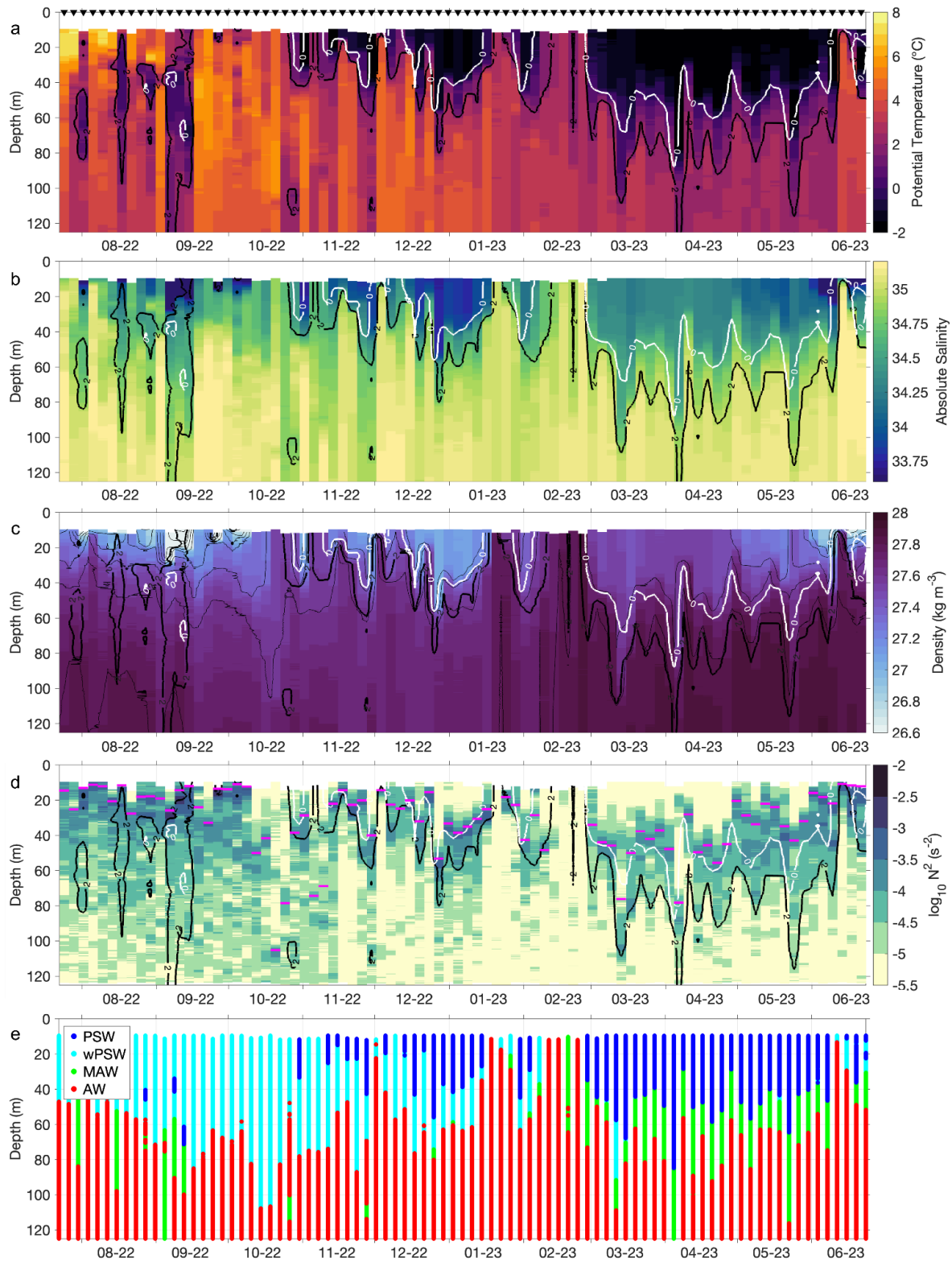


**Figure 4.** Timeseries of profiles of (a) potential temperature, (b) absolute salinity, (c) potential density anomaly, (d) stratification ( $N^2$ , plotted logarithmically), and (e) distribution of water masses, as measured by the winch from July 2022 to June 2023. The pink line in (c,d) is the mixed layer depth (MLD). Note that there are profiles which are well mixed throughout the measured range indicating that the mixed layer was likely deeper than the lowest

*measurement; in this case we do not plot the pink line for the MLD. In all panels, the 0°C and 2°C isotherms are the labelled white and black contour lines, indicating Atlantic Water and Polar Water respectively. The black triangles in (a) indicate the timing of each profile. Acronyms are water masses defined by Rudels et al (2000) and in Table 2; warm Polar Surface Water (wPSW), Polar Surface Water (PSW), Atlantic Water (AW), and Modified Atlantic Water (MAW).*

From November until June, near-surface temperatures declined towards the freezing point, reaching within 0.2°C of the freezing point between March and May (Fig. 3d). Cold and fresh PSW dominated the surface layer, progressively deepening down to a maximum of 80 m depth in April 2023, and wPSW diminished (Fig. 4a,e). A pronounced thermocline and halocline separated the PSW layer from the underlying AW, with an interfacial layer of MAW forming as a result of AW cooling and mixing with PSW, though stratification weakened from November onwards ( $N^2 < 10^{-5} \text{ s}^{-2}$ ) as the AW core cooled. This facilitated the development of a deeper mixed layer which generally spanned between 40 - 60 m depth (Fig. 4c).

A notable hydrographic anomaly occurred in January and February 2023 when the PW surface layer disappeared for approximately 2 weeks in January and nearly all of February. During this period, warm and saline AW reached the near-surface, accompanied by an abrupt shoaling of the MLD to < 20 m (Fig. 4c). These AW events coincided with a sharp reduction in SIC, including a brief ice-free period in February (Fig. 3c). A significant negative correlation ( $R = -0.7$ ,  $P < 0.01$ ) is observed between SIC and ocean temperature at 12 m between October and April with a zero-lag, and a weaker but still significant correlation ( $R = -0.6$ ,  $P < 0.01$ ) between SIC and salinity over the same period (Fig. 3c,d). These correlations suggest that changes in SIC occur with near-simultaneous (<4 days) shifts in near-surface ocean conditions. The PW layer began to thin in mid-May (Fig. 4), while near-surface freshening (Fig. 3d) led to a strengthening of stratification at the AW/PW interface (Fig. 4d). The MLD shoaled significantly, returning to its shallowest state (~20 m) by June (Fig. 4c).

The circulation at the mooring site was characterised by a northeastward (Fig. 5a) and generally barotropic flow (Fig. 5b,c), consistent with AW advection along the continental shelf break (Fig. 1b). The along-slope currents were consistently strongest along the shelf between mid-October and December, reached peak velocities of  $0.3 \text{ ms}^{-1}$  and weakened during spring and summer, almost halting between April and May. Brief southerly flows (~1 week) during this period suggest an episodic transition from along-shore to onshore transport. Alternating bands of positive and negative velocities frequently appeared after January, spanning the depth of the upper water column, and persisted for several days to

weeks (Fig. 5c). These features likely indicate mesoscale structures on the order of 10 - 100 km in diameter (von Appen et al. 2022; Kozlov and Atadzhanova 2021), or may reflect the meandering of the boundary current across the slope (Pérez-Hernández et al., 2019).

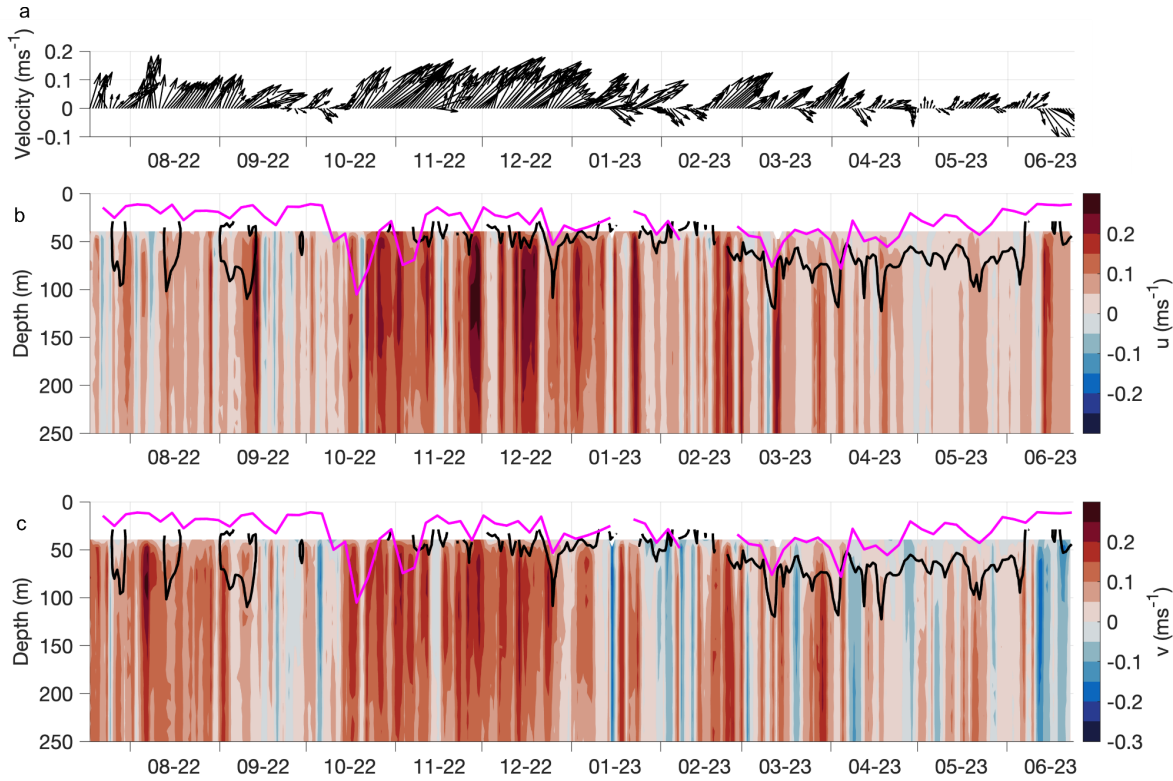


**Figure 5. Flow direction over Yermak Plateau.** Daily averaged (a) quiver vectors averaged over the upper 125 m of the water column, and the (b)  $u$  and (c)  $v$ -component of velocity from the ADCP record at the neighbouring mooring (Y1-1) (Fig. 1b). The 2°C isotherm is the thick black line and the MLD is the pink line. Positive  $u$ -component velocity is towards the east and positive  $v$ -component velocity is towards the north.

### 3.3. Seasonal cycle of hydrographic properties

The upper water column exhibits clear seasonal hydrographic shifts on the Yermak Plateau (Fig. 4). The mooring was deployed and recovered in summer, when temperature-salinity (T-S) variability was most pronounced. Temperatures ranged from below -1.5°C to nearly 8°C, and salinities varied from 33 to over 35 (Fig. 6a). These wide temperature and salinity ranges were concentrated in the upper 50 m, indicating the presence of warm, saline AW and cooler MAW, and colder, fresher water - both PSW and warm PSW (wPSW) which is influenced to a greater extent by the warm AW (Rudels et al. 2005) - in the surface layer (Table 2). In contrast, variability decreased with depth where AW dominated, reflecting the presence of a stable thermocline and halocline.

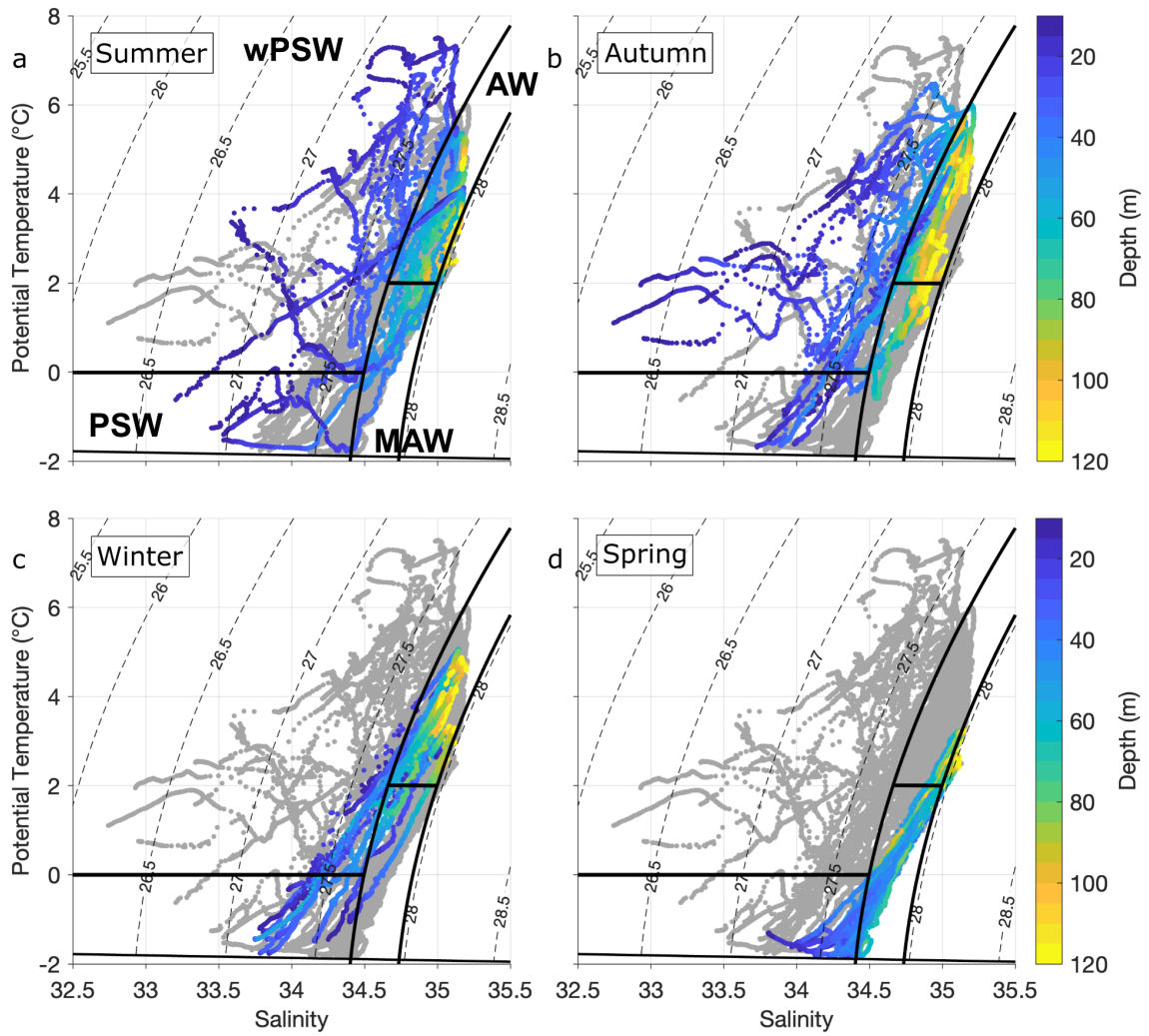


**Figure 6. Seasonal distribution of water masses.** Scatter plots of potential temperature and absolute salinity, aggregated by seasonal groups. (a) Summer (June - August), (b) autumn (September - November), (c) winter (December - February) and (d) spring (March - May). Grey dots show all the available data; coloured dots are observations from the respective season, and the colours indicate depth. Contours are selected isopycnals ( $\text{kg m}^{-3}$ ) used in the definitions of the water masses are indicated (see text for details) and the freezing line is the bold black line at the bottom of each panel. Acronyms are water masses defined by Rudels et al (2000); warm Polar Surface Water (wPSW), Polar Surface Water (PSW), Atlantic Water (AW), and Modified Atlantic Water (MAW).

During autumn, between September to November, the T-S relationship remained highly variable in the near-surface, but with a noticeable shift to colder and fresher conditions in the wPSW compared to summer (Fig 6b). Maximum temperatures were found below 50 m, peaking at over 6°C, and the AW core deepened. This spread reflects the transition to winter

conditions as surface waters cooled and the summer stratification gradually broke down (Fig. 4a,d).

Winter was characterised by narrower T-S properties, with almost no wPSW and low near-surface PSW temperatures approaching the freezing point. The upper 50 m salinity range was also narrow and suggests limited freshwater inputs during this period (Fig. 6c). In spring, from March to May, the T-S properties shifted towards colder and less variable conditions, almost exclusively PSW and MAW (Fig. 6d). Temperature maxima of  $\sim 3^{\circ}\text{C}$  were found between 50 - 120 m, and water down to 60 m approached the freezing line, indicating well-mixed conditions between the AW and PSW. The reduced variability, particularly in salinity, compared to other seasons is indicative of the weak stratification during this season (Fig. 4d).

### 3.4. Mixed layer depths

The seasonal evolution of the upper ocean stratification strongly influenced the mixed layer depth (MLD). From July to September, the mixed layer remained shallow, generally confined to the upper 30 m and in the wPSW layer (Fig. 4a,b). These shallow mixed layers are consistent with the strong near-surface stratification (Fig. 4d), likely driven by the warmer air temperatures and surface freshening due to sea ice melt (Fig. 3). Stratification weakened with the transition into winter, resulting in a progressive deepening of the MLD which reached  $\sim 80$  m in April (Fig. 4c). During this period, the mixed layer became colder and more saline, composed of PSW (Fig. 4e), reflecting the influence of sustained atmospheric cooling and increased sea ice coverage (Fig 3).

To better understand the drivers of MLD variability and the role of sea ice in mediating atmospheric forcing, the relationship between wind forcing and the MLD across different SIC regimes is examined (Fig. 7). The SWIPS profiler's high-resolution observations are used to examine whether stronger wind forcing leads to deeper MLDs, and how this relationship may be modulated by the presence of sea ice. SIC conditions are classified into three regimes - open water ( $\text{SIC} < 10\%$ ), partial ice cover ( $10 - 80\%$ ), and full ice cover ( $> 80\%$ ). The theoretical Ekman depth is used as a proxy for the potential wind-driven mixing depth (e.g., (Peralta-Ferriz and Woodgate, 2015)), where greater Ekman depths suggest larger potential for wind-driven mixing and thus deepening of the mixed layer.

In open water conditions, typically during summer and early autumn (July - October), the MLD remained shallow ( $< 20$  m), coinciding with the strong near-surface stratification (Fig. 4d), and weak winds and shallow Ekman depths ( $< 40$  m) (Fig. 7). A significant correlation

between the MLD and Ekman depth ( $R = 0.5$ ,  $P < 0.01$ ) during this period suggests that wind-driven mixing is an important control on MLD when sea ice is absent. Notably, in October, the MLD deepened rapidly to over 100 m in ~ 2 weeks (4 profiles). This period coincided with a prolonged strengthening of northerly winds (Fig. 3a) which almost doubled the Ekman depth from 20 m to 40 m (Fig. 7) and temporarily eroded the near-surface stratification (Fig. 4d). This abrupt and rapid deepening of the MLD highlights the dominant role of wind forcing in controlling MLD during ice-free conditions.

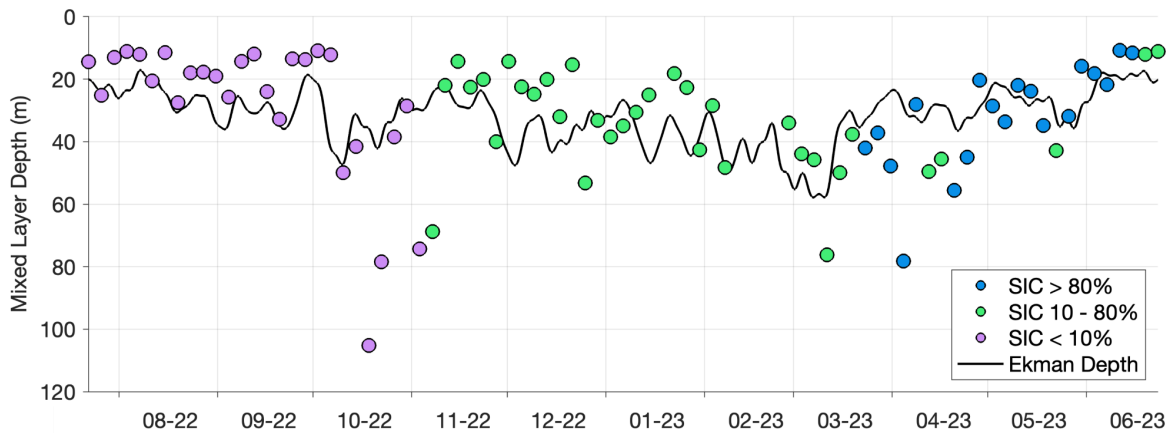


**Figure 7. Connection between wind speed and MLD under different ice regimes.**

Timeseries of mixed layer depth (MLD) for periods of high (> 80%, blue), medium (between 10 - 80%, green) and low (< 10%, purple) sea ice concentration. The black line is the low-pass filtered Ekman depth with a 4-day cut-off period to agree with the winch sampling.

As SIC increased to partial cover (10 - 80 %) between November and March, MLD tended to deepen over time, from ~ 15 m to over 50 m. Higher wind speeds during this time (Fig. 3a) also deepened the Ekman depth over a similar range. Although weaker, the continued correlation between MLD and Ekman depth ( $R = 0.4$ ,  $P < 0.01$ ) suggests that wind-driven mixing still contributes to MLD variability even in the presence of sea ice. The weaker stratification (Fig. 4d) likely allowed the wind-driven mixing to penetrate deeper into the water column. As momentum transfer from the atmosphere to the ocean is most efficient in the presence of partial sea-ice (Martin et al., 2016), thus an increased drag coefficient, it is likely that the Ekman depth in these conditions may be an underestimate. The impact of sea-ice drift and drag on upper ocean processes is further discussed in Section 4.1.

During the period of full ice cover (> 80%), predominantly from April to June, the MLD remained relatively deep, generally exceeding 30 m. Despite fluctuating wind forcing, Ekman depths remained between 20 - 30 m. A weak but statistically significant correlation between MLD and Ekman depth ( $R = 0.3$ ,  $P < 0.05$ ) suggests that wind forcing may exert some

influence on mixing depth, although this influence appears limited. This supports the findings of Peralta-Ferriz and Woodgate (2015) who found that in high SIC regimes, wind is no longer the dominant control on MLD. Instead, convective mixing driven by rejection during sea ice formation likely becomes the primary mechanism for driving the deepening of the mixed layer.

### 3.5. Biogeochemical characteristics

Related to the observed seasonal shifts in hydrography and mixed layers, the biogeochemical properties of the upper water column also exhibit pronounced seasonal and subseasonal variability. From July to mid-September, dissolved oxygen concentrations peaked near the surface ( $> 350 \mu\text{mol l}^{-1}$ ) before decreasing with depth to less oxygenated waters below (Fig 8a). Elevated near-surface chlorophyll fluorescence (Chl-a), typically  $> 1 \mu\text{g l}^{-1}$  and a maximum of over  $3 \mu\text{g l}^{-1}$  (Fig 8c), indicating that a bloom was already underway when the mooring was deployed in mid-July. The depth of the chlorophyll maximum generally followed the MLD which was confined to the upper 30 m. During the bloom period, negative apparent oxygen utilisation (AOU) above 40 m (i.e., oxygen supersaturation) indicated near-surface primary production has raised oxygen concentrations above saturation while positive AOU (i.e., under-saturation from remineralization) occurred below (Fig. 8b). Moderate backscatter in the surface layer supports active biological production (Fig 8f).

CDOM concentrations were also elevated during the summer - not confined to the surface but instead found at mid-depths within colder and fresher MAW intrusions (Fig. 8e). CDOM can also serve as an indicator of freshwater sources in the Arctic system and, as CDOM is commonly enriched in riverine freshwater, these high concentrations indicate that the mid-depth bands of freshwater likely have a large riverine component - potentially originating from Siberian river discharge transported via the Transpolar Drift. Strongly positive AOU values in the mid-depth freshwater parcels support this interpretation, indicating under-saturation and water that has been out of contact with the atmosphere for an extended period. In contrast, the upper  $\sim 30$  m showed lower CDOM concentrations, suggesting it was likely to be less impacted by riverine input.

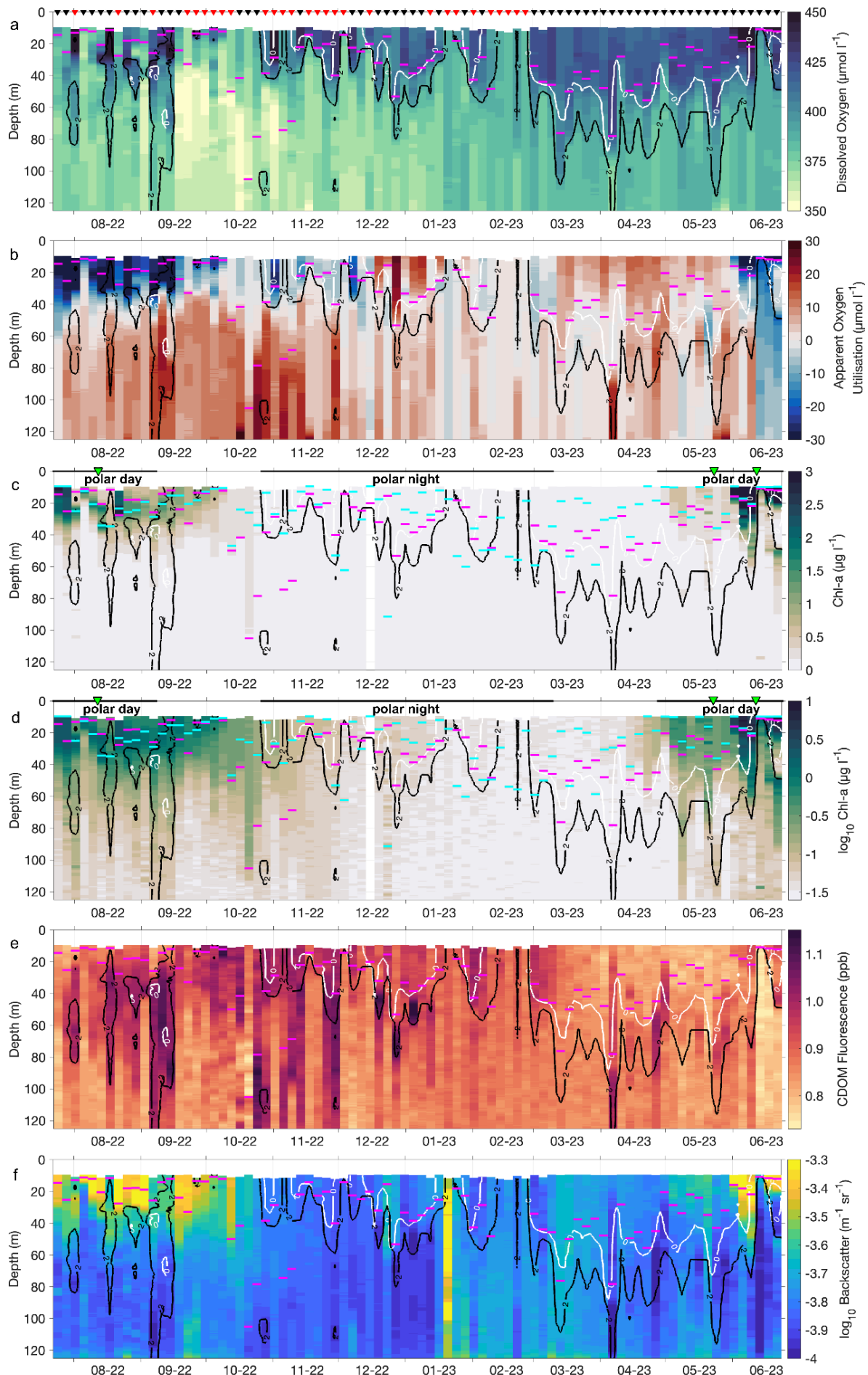


**Figure 8.** Timeseries of biogeochemical properties of (a) dissolved oxygen, (b) apparent oxygen utilisation, (c,d) chlorophyll (Chl-a, linear and log10 scale respectively), (e) CDOM fluorescence, and (f) backscatter (log10 scale) as measured by the winch from July 2022 to June 2023. In all panels, the 0°C and 2°C isotherms are the labelled thick white and black lines, indicating Atlantic Water and Polar Water respectively. The pink lines are the mixed layer depths for each profile. In (c,d), the cyan lines are the depths of the chlorophyll maximum and the three green triangles at the top of the panel are the three profiles in Fig. 11. The length of the polar day and polar night are labelled. The triangles in (a) indicate the location of each profile, and are coloured red if the profiles were vertically interpolated.

In mid-September, near-surface oxygen dropped rapidly between two consecutive profiles (4 days) and remained low throughout the water column until late October (Fig. 8a). Chl-a, AOU and backscatter declined more gradually, tending towards zero by early November (Fig. 8b,c,f). Chl-a remained detectable at low concentrations for over 2 weeks after the onset of Polar Night, suggesting lingering biological activity. Notably, in early October, an abrupt deepening of the MLD towards 100 m redistributed Chl-a throughout the upper water column and likely contributed to the apparent decline in surface fluorescence, though the depth of the chlorophyll maximum remained in the upper 40 m.

Between November and May, during the Polar Night, biogeochemical conditions remained relatively stable. Dissolved oxygen increased in the surface PW layer while subsurface values stayed low (Fig. 8a), and Chl-a remained near-zero throughout the water column (Fig. 8c). By mid-December, AOU in the PW shifted from supersaturated (negative) to undersaturated (positive) values (Fig. 8b), suggesting that the respiration processes that occurred in the bloom in the months prior consumed oxygen since the water was last in equilibrium with the atmosphere. The shift coincided with SIC reaching ~80% (Fig. 3c), indicating that the sea-ice cover likely limited the atmosphere-ocean oxygen exchange to the upper water column. A brief decrease in near-surface AOU towards zero in January and February coincided with a short period of ice-free conditions (Fig. 3c), indicating that the air-sea gas exchange fluxed oxygen into the water column and thus increased oxygen concentration at the surface.

Backscatter also remained low through November to May except for a brief increase in mid-January that was captured by a single profile (Fig. 8f). As Chl-a and CDOM behaved consistently and showed no corresponding peaks, this spike is likely not an instrument malfunction. The elevated backscatter likely reflects enhanced particulate matter, possibly from resuspended sediments or material released from melting sea ice rather than new

biological production. Supporting this, anomalously warm ( $> 2^{\circ}\text{C}$ ) near-surface temperatures were recorded at this time (Fig. 3d), consistent with direct ice melt. Additionally, CDOM concentrations remained stable and relatively low (Fig 8e) suggesting the lower salinity surface layer originated from a different source than the CDOM-rich freshwater intrusions observed at mid-depths in August and September - most likely meltwater from sea ice melt which is typically low in CDOM.

In April, biogeochemical conditions began to shift. Chl-a in the upper 40 m increased from mid-April onward, marking the onset of the spring bloom more than a week before the beginning of the Polar Day (Fig. 8d). Chl-a concentrations progressively increased, exceeding  $6 \mu\text{g l}^{-1}$  by early June. While these Chl-a concentrations may vary depending on community composition by a factor of  $\sim 2$  (Roesler et al., 2017), the progression was consistent with the initiation of a mixed-layer regime bloom as described in von Appen et al. (2021) for the upstream Hausgarten observatory's eastern/central Fram Strait location. Elevated backscatter during this period supported an increase in phytoplankton biomass (Fig. 8f). Concurrently, negative AOU values through the water column indicated oxygen supersaturation, meaning that the primary production of the bloom elevated the oxygen concentrations above saturation levels (Fig. 8b). Although SIC remained  $> 60\%$  during this time (Fig. 3c), thus limiting the exchange of oxygen from the atmosphere with the near-surface, the biogeochemical signals indicate a strong biological response to the improving light conditions.

## 4. Discussion

### 4.1. Wintertime Disruptions to Stratification: Convection and Advection of Atlantic Water

During the winter months, the typical stratified structure over the Yermak Plateau - characterised by cold, fresh PW overlying warm, saline AW (Fig. 4) - was abruptly disrupted. For over 3 weeks in February 2023, AW reached the ocean surface, coinciding with a complete absence of sea ice at the mooring location (Fig. 3c). A similar but shorter anomalous intrusion occurred in late January; here, we focus on the more pronounced February event. This disruption to the expected winter hydrographic conditions is likely a result of local convection mixing warm AW upward or horizontal advection transporting AW into the region via the Svalbard Branch. The SWIPS profiler, with its high vertical resolution, offers a rare opportunity to investigate the relative roles of these two processes.

To assess whether local convective winter-time mixing was responsible for the AW reaching the surface, temperature-salinity (T-S) profiles before, during, and after the February event were examined and demonstrated a marked evolution in stratification (Fig. 9). Prior to the AW surface intrusion the water column remained stratified, with a distinct cold and fresh PSW overlaying warm, saline MAW and AW centred below 60 m. However, between 30 January and 3 February, the upper 50 m cooled by approximately  $0.5^{\circ}\text{C}$  and increased in salinity by 0.1, suggesting surface layer modification - possibly through gradual heat loss or weak vertical mixing.

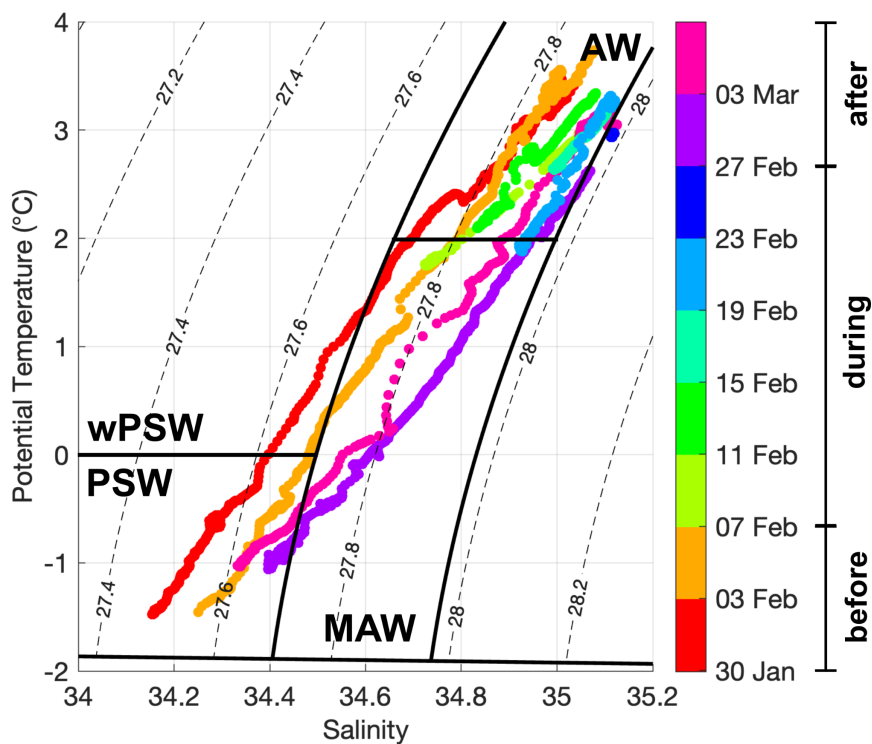


**Figure 9. Water column properties during the AW event in February.**

Temperature-salinity (T-S) plot of profiles from before, during and after AW appears at the surface in February 2023 (see Fig. 4a). Contours are selected isopycnals ( $\text{kg m}^{-3}$ ) used in the definitions of the water masses are indicated (see text for details) and the freezing line is the bold black line at the bottom of each panel. Acronyms are warm Polar Surface Water (PSWw), Polar Surface Water (PSW), Modified Atlantic Water (MAW), and Atlantic Water (AW), defined in Table 2.

By 7 February and the first profile during the AW event, this stratification had collapsed. The T-S properties through the whole upper water column had shifted to AW, indicating a complete disappearance of PSW and MAW. During the early stages of the AW event, on 7 and 11 February, AW temperatures cooled slightly but the salinity range remained similar to

that of the AW core from before the event. This cooling without significant freshening suggests that surface-driven convection, expected to have mixed the AW with fresher PSW, was not the dominant mechanism for the AW surfacing. Later profiles during the AW event showed a narrow T-S range as AW temperatures continued to cool by  $\sim 0.2^{\circ}\text{C}$  and become more dense, indicating local convective mixing and homogenisation of the AW.

Assuming that the MLD extended deeper than the SWIPS winch (Fig. 7), the total mixed layer heat content over the AW event peaked at over  $2 \text{ GJ m}^{-2}$ , corresponding to a positive ocean heat flux exceeding  $6.5 \text{ kW m}^{-2}$  that could be fluxed from the ocean to the atmosphere or, if present, ice lower boundary (Supplementary Figure 3b,c). This flux could theoretically melt over 20 m of sea ice if fully directed at the ice base, without accounting for losses to the atmosphere, yet near-surface salinity did not decline in line with the expected freshwater input from such a scenario (Fig. 3d). Instead, the ice-free conditions likely resulted from suppressed ice formation due to the elevated ocean heat as well as the persistent southeastward sea ice advection (Supplementary Figure 6) that would have prevented new ice formation at the mooring site. Thus, while convection likely contributed to AW modification during the event, it cannot fully explain the timing and magnitude of the anomaly. Note that the MLD heat budget assumes no lateral advection of heat which simplifies interpretation of vertical fluxes but may underestimate or overestimate the ocean-to-atmosphere heat flux during periods of strong boundary current activity.

The cooling of the AW could also indicate that deeper vertical mixing or upwelling brought deeper, colder AW to the surface. Although no hydrographic data are available below the SWIPS winch at the mooring location (Fig. 2), the adjacent Y1-1 mooring (Fig. 1b) was equipped with deeper instruments (Table 1). A significant correlation between temperature measurements from the two moorings at 100 m ( $R = 0.8$ ,  $P < 0.01$ , Supplementary Figure 4) suggests that Y1-1 can be used as a reasonable proxy. The temperature measurements at 250 m showed only a  $\sim 0.1^{\circ}\text{C}$  difference compared to the overlying AW during the event, making deep upwelling an unlikely cause of the observed total  $> 1^{\circ}\text{C}$  cooling of the AW (Fig. 9). Thus, while local convection appears to have modified the AW, it is unlikely to be the dominant mechanism for initiating the AW event.

Alternatively, the advection hypothesis suggests that the observed AW intrusion at the surface in February was primarily driven by horizontal transport of AW from the south, likely via the Svalbard Branch (Fig. 1a). Supporting this, the T-S characteristics of the surface layer during the AW event closely resembled the AW core observed at depth beforehand with minimal salinity variability, indicating minimal local mixing with the PSW (Fig. 9). Instead,

the surface layer aligned with the mixing line of the existing AW core, suggesting that the AW during the event was advected from a region already dominated by AW rather than formed in-situ from local convection. The rapid recovery of stratification following the AW event, as PSW re-established and the AW core deepened below 60 m (Fig. 4e), further reinforces that this was driven by a temporary shift in oceanographic conditions such as advection and not due to a sustained change in winter hydrography.

Sea surface temperature (SST) maps trace the pathway of warm surface waters that reached the mooring site in early February, coinciding with the onset of AW-dominated conditions. In January, before the AW event, the mooring site was located near the ice edge and surrounded by colder PSW (Fig. 10a). In early February, warm AW advanced northward, following the Svalbard continental shelf edge (Fig. 10b-d) and reached the mooring site by 7 February - precisely when AW-dominated conditions first appeared at the near-surface (Fig. 4). These SST observations trace a clear path of AW transport from the WSC toward the Yermak Plateau. This timing is also consistent with the expected advection timescales. The WSC core flows at  $0.15 - 0.2 \text{ ms}^{-1}$  (McPherson et al. 2025 - this issue), such that an AW anomaly could travel from the WSC mooring array in Fram Strait at  $79^\circ\text{N}$  to the SWIPS site within 10 - 14 days if transported via the more direct pathway across the Yermak Plateau and the flow speed was maintained. The onset of warm conditions at the mooring site occurred within that window relative to upstream SST changes, supporting advection as the dominant driver of the AW event.

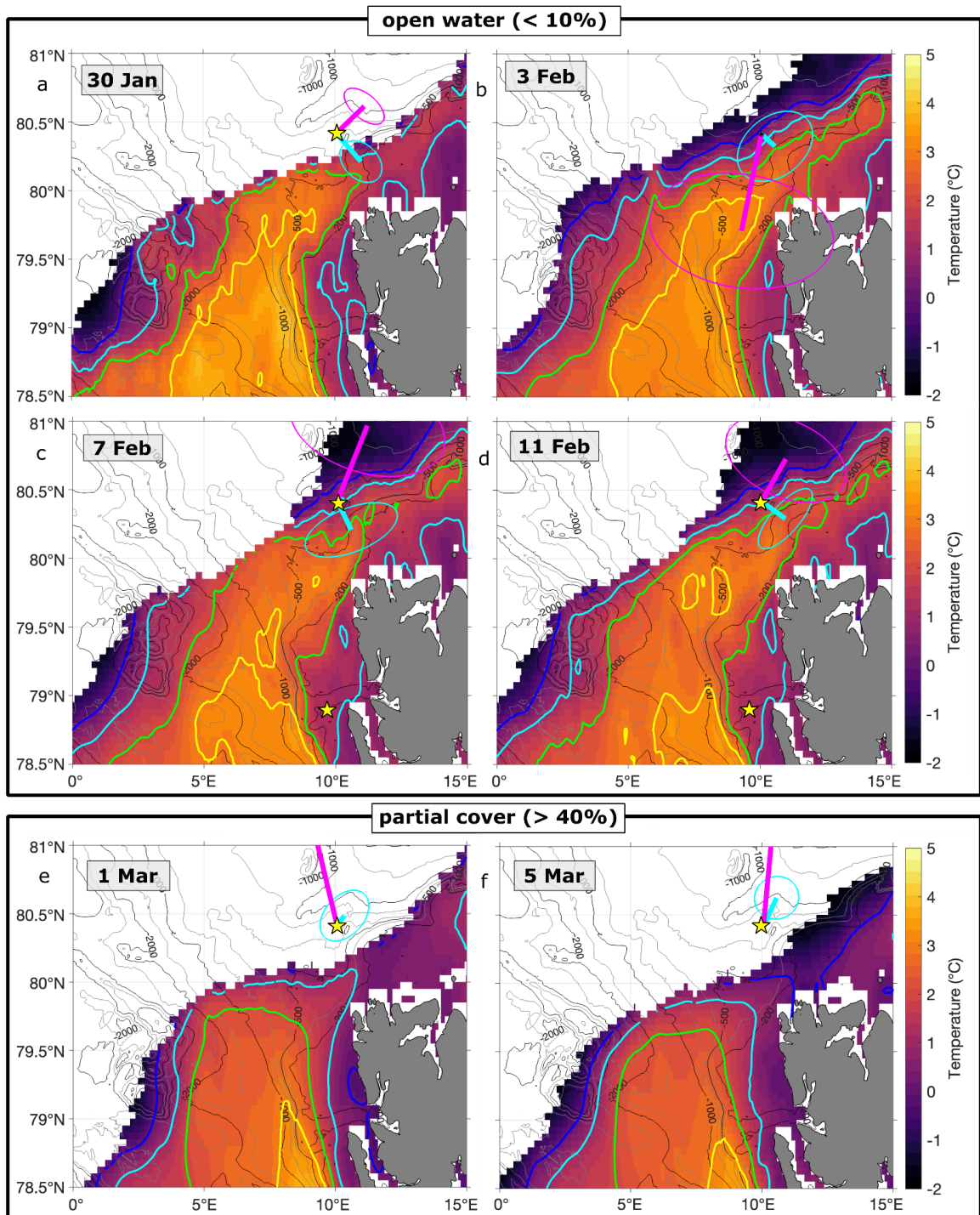


**Figure 10: Northwards advection of AW.** SST maps on specific days (a - d) around the ice-free period in February 2023, and (e,f) in early March when SIC had increased again to above 40%, with the Y1-1 mooring (located 1.5 km south of Y2-1 which contained the winch) marked (yellow star). The 0°C isotherm is marked in blue, the 1°C isotherm is cyan, the 2°C isotherm is green, and the 3°C isotherm is yellow. Centred on the Y1-1 mooring are mean ocean current speeds and direction at 50m (cyan) and wind speed and direction (pink), averaged over a 3-day window and both in the oceanographic direction (i.e., pointing

*towards the direction of flow). The white area in each map is ice-covered thus no data is available.*

A deviation in ocean current direction from the typical northeastward flow along the shelf to a southeastward current also occurred during the AW event (Fig. 10, Supplementary Figure 6). This coincided with a shift in wind direction towards the northeast, meaning the observed onshore current was approximately 90° clockwise from the wind direction and consistent with expected wind-driven Ekman transport. This alignment indicates that the local wind forcing likely contributed to both the onshore transport during the AW event and the northeast advection of AW from the WSC around the northern tip of Svalbard. The effectiveness of this wind forcing, however, is closely linked to the mobility of the sea ice cover which controls how wind stress is transferred to the ocean. In the Yermak Plateau region, where the sea ice is mobile rather than land-fast, the wind stress can reach the ocean surface and drive vertical momentum transfer and mechanical mixing. This can erode stratification, generate inertial oscillations, and enhance upper ocean variability (Fer et al. 2010). The partial ice conditions and strong winds both during the AW event and through the year (Fig. 3a,c) likely enabled more efficient transmission of wind energy into the ocean, contributing to the observed variability in MLD (Fig. 7) and modulating the advection and vertical structure of AW (Fig. 5, 9). While the efficiency of this wind stress transmission through sea ice can be characterised by the “wind factor” - which varies with ice thickness, drift speed and oceanic forcing (Gebhardt et al., 2010) - it is not explicitly calculated here and instead assumed that the observed ice mobility during the AW event was sufficient to transmit the wind stress. This assumption is supported by the corresponding current response (Fig. 11) and MLD variability (Fig. 7). Nonetheless, we acknowledge that sea ice drift complicates the interpretation of atmospheric forcing as circulation and mixing in the region are also strongly influenced by oceanic processes and topographic effects. Baroclinic instabilities of the Svalbard Branch and tidal forcing generate mesoscale eddies and internal waves that interact with ice dynamics, further modifying upper ocean properties (Fer et al. 2010; Artana et al. 2022) and adding uncertainty to the interpretation of wind-driven variability.

These complex interactions between sea ice, wind, and ocean dynamics also help explain the pronounced interannual variability in sea ice concentration on the Yermak Plateau. Previous studies have reported similar brief (1 - 2 weeks) reductions in SIC on the Yermak Plateau during January and February, often following an initial peak in November or December (Lundsgaard et al. 2021; Renner et al. 2018; Koenig et al. 2022). This indicates that the February 2023 AW event was not an isolated anomaly but rather part of a recurring pattern. Furthermore, the findings indicate that sea ice variability in this region is not solely

controlled by upper ocean heat content. While the AW inflow can inhibit ice formation and delay the development of persistent sea ice cover, broader atmospheric and oceanic circulation patterns — including wind forcing and advection — also play a significant role in shaping seasonal sea ice extent and its impact on upper ocean structure.

## 4.2. Deep Chlorophyll Maxima and the Challenges of Observing Arctic Blooms

Seasonal changes in the hydrography shape the conditions that govern phytoplankton growth, particularly in regions with variable stratification and intermittent sea ice cover that can limit light and nutrient availability (von Appen et al. 2021; Sakshaug and Slagstad 1991; Renner et al. 2023). While satellite-derived Chl-a are widely used to track the large-scale bloom development in the Arctic Ocean, they remain limited in their ability to resolve subsurface features or detect under-ice blooms, both of which can represent significant fractions of total biomass (Kahru et al. 2016; Ardyna et al. 2020; Bouman et al. 2020). Satellites also only capture near-surface Chl-a within the first optical depth - varying regionally from 5 m to 30 m at the mooring location - but not the vertical extent of phytoplankton distribution. Additionally, their coarser spatial resolution (4km by 4km for the matchup with the GlobColour dataset used in this study), compared to in-situ observations, may mask localised blooms. In contrast, the high-resolution vertical profiles collected year-round by the SWIPS profiler tracks the full seasonal evolution of phytoplankton across the upper water column, independent of sea ice cover and cloud conditions. This enables a unique detection of subsurface maxima and at temporal frequency that is capable of resolving short-lived transitions in bloom regimes that would be otherwise missed by surface-based remote sensing, especially during the shoulder seasons when light is increasing but surface melt and SIC remain variable.

Individual SWIPS profiles demonstrate the profilers' ability to resolve fine-scale vertical structure up to the near-surface in varying ice conditions. The profiler captured a subsurface Chl-a maximum at 22m, nearly 10m below the MLD in ice-free conditions during the 2022 bloom (Fig. 11a) and while under high SIC (> 80%), the profiler captured a subsurface Chl-a maximum that shifted with the mixed layer depth (Fig. 11b, c). Observing near-surface ocean conditions are particularly challenging in the Arctic, where moorings are typically designed to avoid ice damage, leading to sensor placements deeper in the water column. von Appen et al. (2021) demonstrated that for the meltwater regime in the Hausgarten area, thin highly concentrated layers of chlorophyll residing in the strong meltwater stratification had to be inferred indirectly due to the depth constraints of moored sensors. By providing direct,

high-resolution vertical coverage, the SWIPS profiler eliminates the need for interpolation and/or indirect inferences.

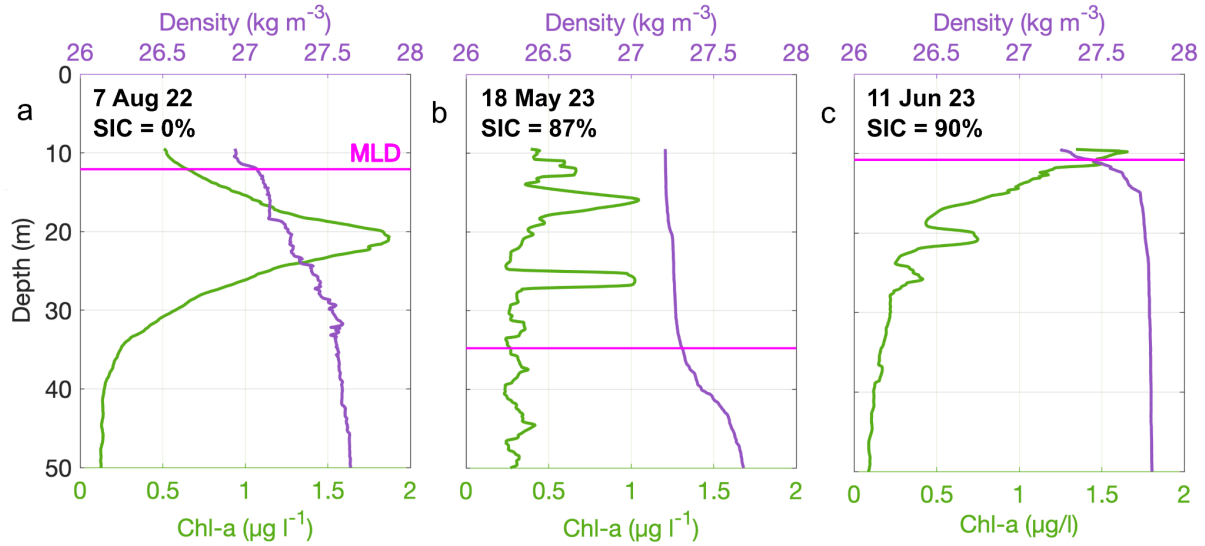


**Figure 11.** Selected profiles of chlorophyll fluorescence (green), density (purple) and corresponding mixed layer depth (MLD) (pink). The date and sea-ice concentration (SIC) at the time of the profile are given in each panel.

The SWIPS observations also show that during both the autumn bloom of 2022 and the onset of the 2023 spring bloom, the subsurface Chl-a maximum was generally located at, or just below, the MLD (Fig. 12b), and these subsurface chlorophyll maxima often contained chlorophyll concentrations several times higher than the near-surface waters (Fig. 12a). The vertical structure observed in the profiles (Fig. 11) further emphasises that phytoplankton biomass cannot be accurately represented by a single maximum value alone, and a single surface Chl-a value can significantly misrepresent total phytoplankton biomass. Vertical integrations of chlorophyll profiles also frequently reveal biomass that are an order of magnitude higher than surface estimates alone (Fig. 12a). This discrepancy reflects both the vertical redistribution of biomass, likely influenced by stratification and light availability, and the inability of satellite sensors to resolve fine-scale or subsurface biological structure. The profiling of SWIPS allows for a more complete temporal and vertical picture of bloom development, meaning that total phytoplankton biomass in the upper ocean is often underestimated when only surface or near-surface concentrations are considered.

The importance of resolving vertical resolution in assessing bloom dynamics is further evident in comparisons between SWIPS and satellite-derived chlorophyll estimates. In 2022, both datasets captured the broad timing and seasonal trend of the bloom period from July to September and showed a statistically significant correlation in Chl-a concentrations ( $R = 0.5$ ,

$P < 0.05$ ) (Fig. 12a). However, satellite-derived concentrations were consistently lower, with peak values reaching only  $\sim 0.5 \mu\text{g l}^{-1}$  compared to  $\sim 2.5 \mu\text{g l}^{-1}$  in the in-situ data. These differences are likely due in part to the GlobColour gap-filling approach that replaces missing values with climatological means and can obscure short-term variability (Supplementary Figure 5). From mid-September, when satellite data ceased due to insufficient ambient light for the passive measurement, the SWIPS profiler documented a steady decline in Chl-a towards  $0.1 \mu\text{g l}^{-1}$  when the near-surface and maximum values became comparable (Fig. 12a).

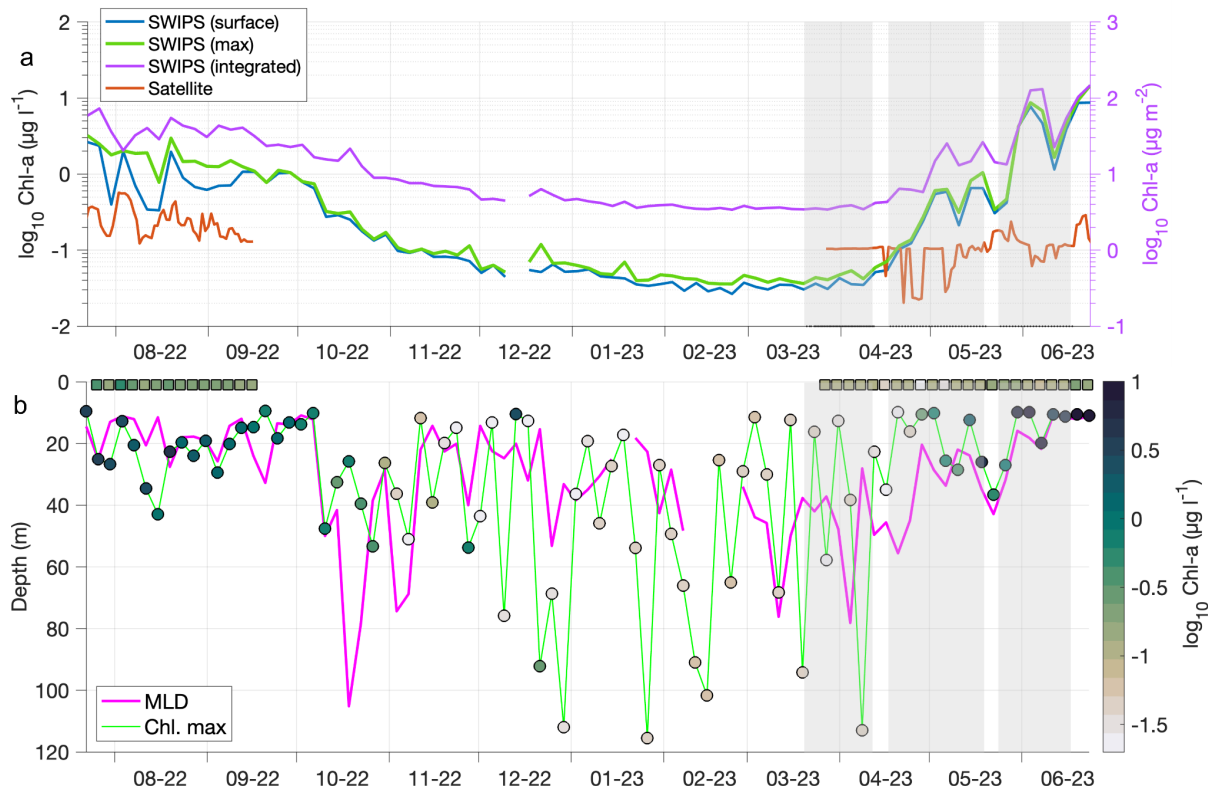


**Figure 12: Near-surface chlorophyll.** Timeseries of  $\log_{10} \text{Chl-a}$  (a) at the near-surface (12m, blue), maximum sub-surface (green), and integrated over the depth of each profile (purple) as measured by the SWIPS, and satellite-derived daily Chl-a (orange) averaged from a 12 km square centred about the mooring; (b) depth of the mixed layer (MLD, magenta) and the depth of Chl-a maximum (thin green line), with the maximum Chl-a value from the SWIPS profiler imposed on top as colored circles. The corresponding satellite Chl-a values are also included at the surface (squares). Grey shading in both panels is the time when SIC > 80%.

The 2023 spring bloom showed even greater divergence. Although both satellite and in-situ measurements identified an overall increase in chlorophyll beginning in April–May, the SWIPS detected a clear subsurface peak in mid-April, nearly two weeks before the satellite

product indicated bloom onset. The discrepancy is likely tied to sea ice conditions. At the end of the 2022 bloom (July–August), SIC at the mooring location was low (< 10%) whereas during the onset of the 2023 bloom, high SIC (> 80%) may have impeded the satellite's ability to detect the early signals (Fig. 3c). A sharp chlorophyll peak (~6.2  $\mu\text{g l}^{-1}$ ) measured in early June by the SWIPS profiler was entirely missed by the satellite product which showed a decrease in concentration at that time (Fig. 12a). Only in late June, as SIC declined, did both datasets align in identifying a Chl-a peak, though satellite estimates remained an order of magnitude lower than the in-situ measurements. The early increase of Chl-a in April 2023 suggests that sufficient light penetrated through the sea ice (with concentrations > 80%, Fig. 3c) to support phytoplankton growth, which is perhaps unsurprising given that 50% SIC still means that half of the water surface is exposed to the atmosphere and sea ice can, at a maximum, reduce half of the incoming light relative to open water. These observations indicate that under-ice phytoplankton blooms can develop well before complete ice retreat, aligning with recent findings that under-ice blooms contribute significantly to Arctic primary production (Ardyna et al., 2020).

Overall, while satellite-derived Chl-a captures broad seasonal trends, it consistently underestimates peak concentrations, particularly during peak bloom periods when phytoplankton tend to be concentrated at depth. Note that the fluorescence-to-Chl-a conversion used for the SWIPS in-situ estimates also has some uncertainty, typically within a factor of 2 (e.g., von Appen et al. 2021; Roesler et al. 2017). No correction was applied for potential quenching of the near-surface fluorescence signal which can suppress near-surface fluorescence under high light conditions and lead to underestimation of chlorophyll concentrations (Mitchell et al., 2024). However, the SWIPS profiles began at ~12 m depth, reducing sensitivity to this effect that is strongest in the upper few meters. Additionally, persistent daylight in the Arctic summer likely minimizes strong diurnal variability in quenching. While some underestimation of near-surface Chl-a is possible, these effects cannot explain the order-of-magnitude discrepancies observed between in-situ and satellite-derived chlorophyll estimates. Nonetheless, future validation with discrete water samples will be important to better constrain fluorescence-based estimates and quantify any bias. The inability of satellite sensors to detect short-lived Chl-a spikes, particularly during periods of rapid bloom onset, may stem from multiple factors including their broader spatial coverage, or due to a number of environmental factors such as the obscuring nature of the significant cloud cover in the Arctic (Jouini et al., 2013). Gap-free satellite Chl-a product can also misrepresent the time-being conditions when the climatological data that fills the data gaps doesn't catch the real time variability. Alternative Arctic-tuned satellite datasets, such as CHL-Arc, may provide improved estimates, but have limited temporal coverage

(Supplementary Figure 5). Given the high variability in chlorophyll dynamics observed in Arctic waters, high-resolution in-situ observations, such as those from the SWIPS, are essential to capture fine-scale biological processes and key seasonal transitions such as the onset of the spring bloom and episodic peaks in Chl-a, particularly in regions with intermittent sea ice cover.

Despite the limitations, satellite datasets remain valuable for placing the in-situ local observations in a regional context. The elevated Chl-a concentrations recorded at the SWIPS mooring location in July 2022 were part of a wider regional bloom extending over both 12 km and 100 km around the SWIPS (Fig. 13a,b). The bloom began in mid-May and peaked rapidly, with concentrations exceeding  $2 \mu\text{g l}^{-1}$  within 2 weeks. This pattern aligns with the recorded onset of previous blooms farther upstream in the WSC in 2017 and 2018 (von Appen et al. 2021), indicating that the bloom development in the region is at least partially governed by regional-scale drivers such as the AW inflow, light availability and sea ice conditions rather than local factors. By July 2022, when in-situ measurements began, the peak bloom had already passed and satellite maps indicate that Chl-a concentrations near the mooring location were in decline. A weaker, yet still extensive, bloom signature persisted through August, though mostly concentrated along the continental shelf around Svalbard.

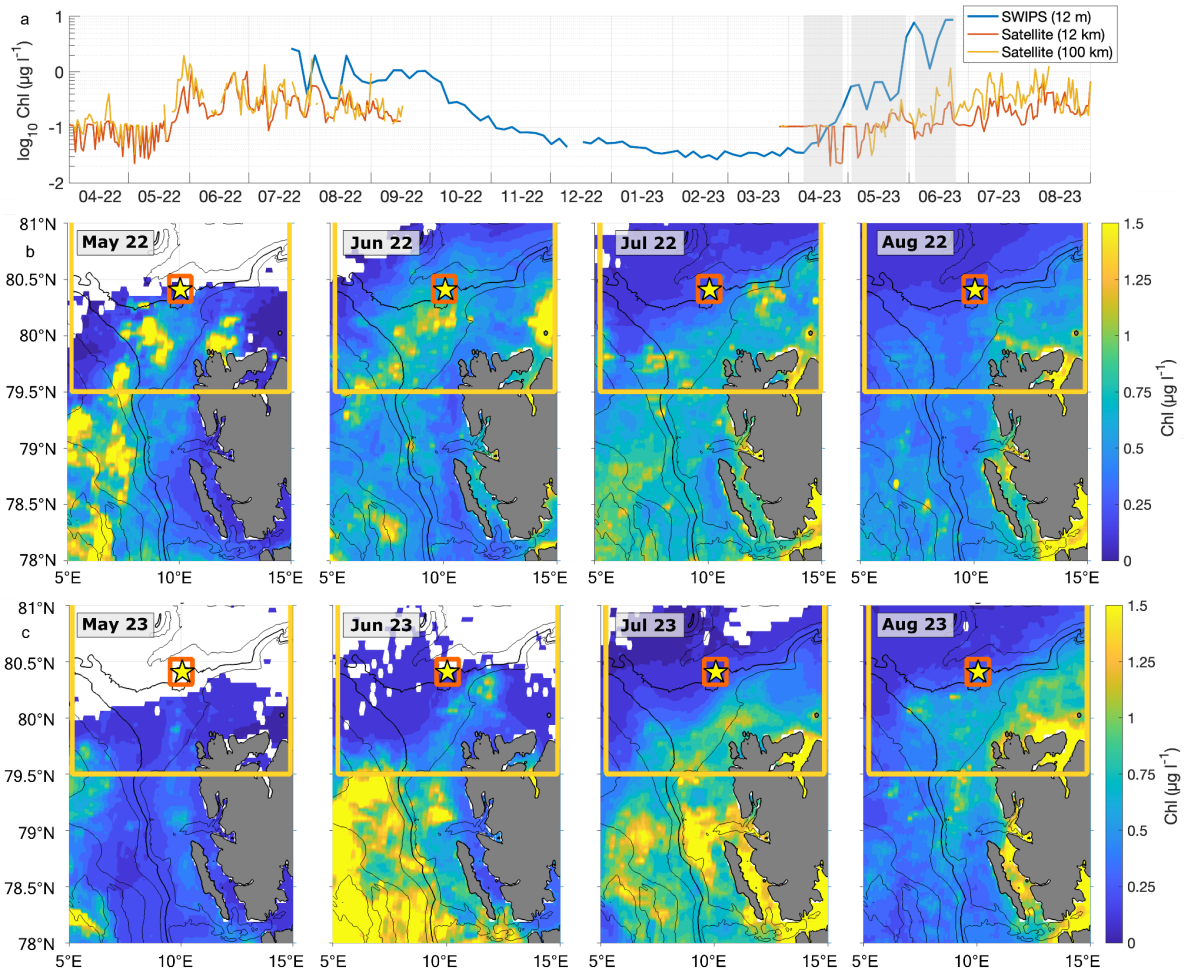


**Figure 13: Regional blooms.** Timeseries of near-surface chlorophyll from the SWIPS at 12 m ( $\text{Chl-a}$ , blue), and satellites averaged over a 12 km (orange) and 100 km (yellow) square centred around the SWIPS mooring location. Maps of satellite-derived monthly chlorophyll  $\text{Chl}$  during the blooms in (b) 2022 and (c) 2023. The SWIPS mooring location is the yellow stars, and the 12 km and 100 km squares centred around the mooring location are the red and orange boxes respectively. Grey shading in (a) is when  $\text{SIC} > 80\%$ .

The onset of the 2023 bloom was, in contrast, delayed and weaker, with peak Chl-a concentrations occurring in mid-June (Fig. 13b). This timing difference may be linked to the influence of higher sea ice concentrations around the mooring in spring 2023 (Fig. 3c, 13a,c) which likely limited light availability in the upper ocean and delayed the onset of stratification favorable for phytoplankton growth and primary productivity (Nicolaus et al., 2012). Renner et al. (2023) also found a direct relationship between sea ice cover and chlorophyll variability in the Yermak Plateau region. Higher SIC was associated with reduced Chl-a concentrations, and an increase in biomass when SIC was low, reinforcing that sea ice conditions can directly influence Arctic bloom timing and magnitude.

## 4.3 Capabilities of a winched profiler for upper ocean observations in the Arctic

Understanding seasonal variability in the Arctic upper ocean requires high-resolution, temporally continuous vertical measurements of hydrographic and biogeochemical structure. Traditional observations - such as oceanographic fixed-depth moorings, ship-based CTD casts, and satellite remote sensing - each provide important measurements and insights but are individually limited: moorings lack vertical resolution, CTD casts are episodic, and satellite data are restricted to the surface and degraded under cloud cover or sea ice coverage. To fill each of these gaps, the data often require interpolation between measurement points to estimate vertical structure or temporal changes. This can lead to uncertainty in capturing fine-scale structures, particularly in highly dynamic or stratified environments such as the MIZ where key processes evolve rapidly in time and space.

In this context, winched profilers such as SWIPS address a critical observational gap by providing regular, high-resolution profiles of the upper ocean throughout the year, including under partial or complete sea ice cover. The profiler resolved temporary shifts in near-surface oceanographic conditions driven by advection and deep mixing events (Fig. 4, 9), short-term variability in MLD (Fig. 7), and subsurface chlorophyll maxima (Fig. 11, 12) that would likely be missed by other platforms. For example, the spring bloom of 2023 exhibited a pronounced subsurface chlorophyll peak weeks before satellite remote sensing indicated bloom onset (Fig. 12a). This early biomass accumulation—occurring beneath sea ice and below the surface—is only visible through vertically continuous observations. Satellite remote sensing, while offering valuable broad spatial coverage, cannot detect subsurface features and are frequently compromised by cloud cover or high sea ice concentration. This is particularly problematic during bloom periods, when phytoplankton are often concentrated below the surface, leading to significant underestimation of biological production (Fig. 12,13a). Similarly, abrupt changes in MLD, such as the > 90 m deepening observed over a two-week period in October (Fig. 7), are unlikely to be resolved by traditional moorings or seasonal CTD cruises alone. Moorings, though capable of capturing high-frequency variability, often miss the vertical structure needed to interpret biological or stratification changes (von Appen et al. 2021).

While the 4-day sampling interval captures broad seasonal transitions, shorter-term episodic events—such as mixing or bloom onset—may remain undersampled. Increasing the temporal resolution would improve detection of episodic mixing and rapid biological responses. This need is highlighted by the large profile-to-profile variability in the MLD, most

notably in October when the MLD deepened from 10 m to over 100 m within 2 weeks (4 profiles) (Fig. 7). Moreover, the current profiler reaches to ~10 m from the surface; extending coverage into the upper ~10 m and under-ice boundary layer would enhance the ability to observe air-ice-ocean exchanges, meltwater-driven stratification, and near-surface ecological dynamics, all of which remain poorly resolved.

SWIPS would be most effective when deployed in conjunction with traditional moorings, which provide high-frequency point measurements needed to capture short-term variability, tides, turbulent mixing processes, or rapid bloom initiation. Together, these platforms offer complementary views of the upper ocean, resolving both vertical structure and fine temporal dynamics. Likewise, combining profiler data with satellite observations extends their spatial context, while repeated ship-based sampling continues to provide critical calibration, sensor validation, and biogeochemical measurements beyond current autonomous capabilities.

As Arctic conditions evolve rapidly, maintaining and expanding multi-platform observing systems will be essential. Winched profilers such as SWIPS offer a unique capability to observe fine-scale vertical processes—including those beneath ice cover—that remain inaccessible to other platforms. Their integration into sustained Arctic monitoring efforts will improve understanding of seasonal dynamics, stratification, and ecosystem responses in a changing climate.

## 5. Conclusion

A novel winched profiling system (SWIPS) was deployed in the Atlantic Water (AW) pathway north of Svalbard. From July 2022 to July 2023, the profiler collected 85 high-resolution vertical profiles of hydrographic and biogeochemical properties, spanning from ~125 m to 10 m below the surface at 4- day intervals. The SWIPS profiler captured key seasonal transitions, fine-scale variability, and upper ocean processes that are often unresolved by traditional observational methods. Its ability to profile the upper ocean—particularly the near-surface layer—under both open water and sea ice conditions enabled a uniquely detailed, year-round characterization of Arctic upper ocean structure and productivity.

By resolving vertical structure at high resolution throughout the year, including during the Polar Night and ice-covered periods, SWIPS provided direct observations of evolving water masses, upper ocean stratification, and biological activity. It documented the progression from a warm Polar Surface Water (wPSW) in summer to a colder Polar Surface Water (PSW) layer in winter at the onset of sea ice coverage, separated from the underlying AW by

an interfacial layer of Modified Atlantic Water (MAW) which formed as a result of AW cooling and mixing with the PSW. Seasonal mixed layer deepening was observed during autumn and winter, although high sea ice concentrations (SIC, > 80%) likely limited the wind-driven mixing which was the dominant control on MLD during open water regimes.

SWIPS also captured temporary but impactful anomalies in the upper water column. In January and February 2023, AW reached the surface and disrupted the expected cold, stratified winter regime. The longer of these events in February coincided with a brief ice-free period. Hydrographic profiles, combined with satellite sea surface temperature (SST) maps, indicated that this event was driven by upstream advection of AW from Fram Strait rather than local convection. While ocean heat flux likely contributed to ice loss, the disappearance of sea ice was not solely driven by oceanic heat but was likely influenced by regional atmospheric and oceanic circulation anomalies that enhanced AW transport and displaced sea ice. These findings reinforce the role of remote forcing and oceanic heat transport in shaping upper ocean conditions, ice dynamics, and stratification on synoptic to seasonal timescales.

The high vertical and temporal resolution of SWIPS enables detection of the strong coupling between physical structure and biological response in the Arctic upper ocean, particularly under sea ice. In May 2023, a phytoplankton bloom was observed beneath >80% SIC, marking the onset of the spring bloom more than a week before the beginning of the Polar Day. This under-ice bloom coincided with shallow stratification and increasing light penetration, illustrating how productive conditions can emerge before full ice retreat. These early-season blooms, and the broader vertical structure of phytoplankton biomass are typically missed by satellites. Subsurface chlorophyll maxima were typically located at or just below the mixed layer depth, resulting in a persistent mismatch with surface-confined satellite estimates. During peak bloom periods, satellite-derived chlorophyll concentrations underestimated in-situ values by up to an order of magnitude, due to a combination of prevalent subsurface biomass, cloud cover, sea ice obstruction, and spatial averaging. The ability to resolve these features underscores the importance of vertically resolved, year-round in-situ observations for capturing biological activity and improving our understanding of Arctic primary production.

Together, these results demonstrate the scientific value of winched profilers, particularly in Arctic regions. SWIPS provided a temporally continuous, vertically resolved dataset that captured both gradual seasonal evolution and short-lived anomalies across ice-covered and open-water conditions. As Arctic change accelerates, sustained high-resolution profiling will

be critical for resolving the complex interplay between ocean physics, biology, and sea ice, and for improving satellite-based assessments and biogeochemical models in this sensitive and dynamic environment. Implementing these advancements would further enhance our ability to monitor and understand changes, particularly in the face of Arctic amplification, reinforcing the need for expanded deployments of winched profilers across key Arctic regions.

## Data Availability

The hydrographic and biogeochemical data from the SWIPS profiler on the Y2-1 mooring is publically available at Pangaea at <https://doi.org/10.1594/PANGAEA.974312>. The raw physical data on the Y1-1 mooring is available on Pangaea at <https://doi.org/10.1594/PANGAEA.974309>. The sea ice concentration and thickness data is available at [ftp://ftp.awi.de/sea\\_ice/product/amsr2/](ftp://ftp.awi.de/sea_ice/product/amsr2/), and the sea ice drift data is available at <https://osi-saf.eumetsat.int/products>. The high-resolution sea surface temperature data is available at <https://doi.org/10.48670/moi-00165>. The ERA5 reanalysis is available at <https://cds.climate.copernicus.eu/datasets/reanalysis-era5-single-levels>. This study has been conducted using E.U. Copernicus Marine Service Information for the satellite chlorophyll estimates from different processings as available at <https://doi.org/10.48670/moi-00280>, <https://doi.org/10.48670/moi-00281>, <https://doi.org/10.48670/moi-00282>, and <https://doi.org/10.48670/moi-00292>.

## Acknowledgements

The authors would like to thank the FRAM associated technicians, engineers, and administrators as well as the captains, crews, and scientific parties on the R/V Polarstern cruises PS131 (Grant: AWI\_PS131\_07), PS137 (Grant: AWI\_PS137\_09) and PS143\_2 (Grant: AWI\_PS143/2\_03) who were all instrumental in making these observations possible.

We thank Lars Kaleschke and Stefan Hendricks for providing the sea ice concentration and thickness data, and Thomas Krumpen for providing the sea ice drift data. We thank Torsten Kanzow for helpful discussions and contributions to the development of this manuscript.

The basic developments of the SWIPS winch system were financed by ICOS-D, the German contribution to the “Integrated Carbon Observation System, ICOS” (EU FP7 grant agreement ID: 211574). Further developments and improvements of the components as well as the

construction of additional units were funded by the Helmholtz infrastructure initiative FRAM (“FRontiers in Arctic marine Monitoring”).

This work is funded by the European Union as part of the EPOC project (Explaining and Predicting the Ocean Conveyor). Views and opinions expressed are however those of the author(s) only and do not necessarily reflect those of the European Union. Neither the European Union nor the granting authority can be held responsible for them.

HX's contribution was supported by the Copernicus Marine Service Evolution Project ML-PhyTAO (23138L03D-COP-INNO-SCI-9000) implemented by Mercator Ocean International.

## References

- Aagaard, K., Foldvik, A., Hillman, S.R., 1987. The West Spitsbergen Current: Disposition and water mass transformation. *J. Geophys. Res.* 92, 3778. <https://doi.org/10.1029/JC092iC04p03778>
- Ardyna, M., Arrigo, K.R., 2020. Phytoplankton dynamics in a changing Arctic Ocean. *Nat. Clim. Change* 10, 892–903. <https://doi.org/10.1038/s41558-020-0905-y>
- Ardyna, M., Mundy, C.J., Mayot, N., Matthes, L.C., Oziel, L., Horvat, C., Leu, E., Assmy, P., Hill, V., Matrai, P.A., Gale, M., Melnikov, I.A., Arrigo, K.R., 2020. Under-Ice Phytoplankton Blooms: Shedding Light on the “Invisible” Part of Arctic Primary Production. *Front. Mar. Sci.* 7, 608032. <https://doi.org/10.3389/fmars.2020.608032>
- Artana, C., Provost, C., Ferrari, R., Bricaud, C., Poli, L., Park, Y., 2022. Tides, Internal and Near-Inertial Waves in the Yermak Pass at the Entrance of the Atlantic Water to the Arctic Ocean. *J. Geophys. Res. Oceans* 127, e2022JC019082. <https://doi.org/10.1029/2022JC019082>
- Athanase, M., Provost, C., Artana, C., Pérez-Hernández, M.D., Sennéchal, N., Bertosio, C., Garric, G., Lellouche, J.M., Prandi, P., 2021. Changes in Atlantic Water Circulation Patterns and Volume Transports North of Svalbard Over the Last 12 Years (2008–2020). *J. Geophys. Res. Oceans* 126, 1–23. <https://doi.org/10.1029/2020JC016825>
- Carmack, E., Polyakov, I., Padman, L., Fer, I., Hunke, E., Hutchings, J., Jackson, J., Kelley, D., Kwok, R., Layton, C., Melling, H., Perovich, D., Persson, O., Ruddick, B., Timmermans, M.-L., Toole, J., Ross, T., Vavrus, S., Winsor, P., 2015. Toward Quantifying the Increasing Role of Oceanic Heat in Sea Ice Loss in the New Arctic. *Bull. Am. Meteorol. Soc.* 96, 2079–2105. <https://doi.org/10.1175/BAMS-D-13-00177.1>
- Cokelet, E.D., Tervalon, N., Bellingham, J.G., 2008. Hydrography of the West Spitsbergen Current, Svalbard Branch: Autumn 2001. *J. Geophys. Res. Oceans* 113, 1–16. <https://doi.org/10.1029/2007JC004150>
- Cole, S.T., Toole, J.M., Lele, R., Timmermans, M.-L., Gallaher, S.G., Stanton, T.P., Shaw, W.J., Hwang, B., Maksym, T., Wilkinson, J.P., Ortiz, M., Gruber, H., Rainville, L., Petty, A.A., Farrell, S.L., Richter-Menge, J.A., Haas, C., 2017. Ice and ocean velocity in the Arctic marginal ice zone: Ice roughness and momentum transfer. *Elem. Sci. Anthr.* 5, 55. <https://doi.org/10.1525/elementa.241>
- Docquier, D., Koenigk, T., Fuentes-Franco, R., Karami, M.P., Ruprich-Robert, Y., 2021. Impact of ocean heat transport on the Arctic sea-ice decline: a model study with EC-Earth3. *Clim. Dyn.* 56, 1407–1432. <https://doi.org/10.1007/s00382-020-05540-8>
- Dumont, D., 2022. Marginal ice zone dynamics: history, definitions and research

- perspectives. *Philos. Trans. R. Soc. Math. Phys. Eng. Sci.* 380, 20210253. <https://doi.org/10.1098/rsta.2021.0253>
- Fer, I., Baumann, T.M., Koenig, Z., Muilwijk, M., Tippenhauer, S., 2022. Upper-Ocean Turbulence Structure and Ocean-Ice Drag Coefficient Estimates Using an Ascending Microstructure Profiler During the MOSAiC Drift. *J. Geophys. Res. Oceans* 127. <https://doi.org/10.1029/2022jc018751>
- Fer, I., Skogseth, R., Geyer, F., 2010. Internal Waves and Mixing in the Marginal Ice Zone near the Yermak Plateau\*. *J. Phys. Oceanogr.* 40, 1613–1630. <https://doi.org/10.1175/2010JPO4371.1>
- Fu, C., Myers, P.G., 2024. Exceptional sea ice loss leading to anomalously deep winter convection north of Svalbard in 2018. *Clim. Dyn.* 62, 2349–2367. <https://doi.org/10.1007/s00382-023-07027-8>
- Hamilton, J.M., Collins, K., Prinsenberg, S.J., 2013. Links between ocean properties, ice cover, and plankton dynamics on interannual time scales in the Canadian Arctic Archipelago: Links in the Arctic Ocean Environment. *J. Geophys. Res. Oceans* 118, 5625–5639. <https://doi.org/10.1002/jgrc.20382>
- Hofmann, Z., Von Appen, W., Kanzow, T., Becker, H., Hagemann, J., Hufnagel, L., Iversen, M.H., 2024. Stepwise Subduction Observed at a Front in the Marginal Ice Zone in Fram Strait. *J. Geophys. Res. Oceans* 129, e2023JC020641. <https://doi.org/10.1029/2023JC020641>
- Jackson, J.M., Williams, W.J., Carmack, E.C., 2012. Winter sea-ice melt in the Canada Basin, Arctic Ocean. *Geophys. Res. Lett.* 39, 2011GL050219. <https://doi.org/10.1029/2011GL050219>
- Johannessen, J.A., Johannessen, O.M., Svendsen, E., Shuchman, R., Manley, T., Campbell, W.J., Josberger, E.G., Sandven, S., Gascard, J.C., Olaussen, T., Davidson, K., Van Leer, J., 1987. Mesoscale eddies in the Fram Strait marginal ice zone during the 1983 and 1984 Marginal Ice Zone Experiments. *J. Geophys. Res. Oceans* 92, 6754–6772. <https://doi.org/10.1029/JC092iC07p06754>
- Jouini, M., Lévy, M., Crépon, M., Thiria, S., 2013. Reconstruction of satellite chlorophyll images under heavy cloud coverage using a neural classification method. *Remote Sens. Environ.* 131, 232–246. <https://doi.org/10.1016/j.rse.2012.11.025>
- Koenig, Z., Kalhagen, K., Kolås, E., Fer, I., Nilsen, F., Cottier, F., 2022. Atlantic Water Properties, Transport and Heat Loss From Mooring Observations North of Svalbard. *J. Geophys. Res. Oceans* 127, e2022JC018568. <https://doi.org/10.1029/2022JC018568>
- Koenig, Z., Provost, C., Sennéchael, N., Garric, G., Gascard, J., 2017. The Yermak Pass Branch: A Major Pathway for the Atlantic Water North of Svalbard? *J. Geophys. Res. Oceans* 122, 9332–9349. <https://doi.org/10.1002/2017JC013271>
- Kozlov, I.E., Atadzhanova, O.A., 2021. Eddies in the Marginal Ice Zone of Fram Strait and Svalbard from Spaceborne SAR Observations in Winter. *Remote Sens.* 14, 134. <https://doi.org/10.3390/rs14010134>
- Laidre, K.L., Heide-Jørgensen, M.P., Nyeland, J., Mosbech, A., Boertmann, D., 2008. Latitudinal gradients in sea ice and primary production determine Arctic seabird colony size in Greenland. *Proc. R. Soc. B Biol. Sci.* 275, 2695–2702. <https://doi.org/10.1098/rspb.2008.0874>
- Lochthofen, N., Frommhold, L., Ludszuweit, J., Soltwedel, T., 2021. A Subsea Winched Profiling System (SWIPS) for Long-Term High-Resolution Measurements in Ocean Surface Layers. *Mar. Technol. Soc. J.* 55, 165–171. <https://doi.org/10.4031/MTSJ.55.2.3>
- Lundsgaard, Ø., Sundfjord, A., Renner, A.H.H., 2021. Drivers of Interannual Sea Ice Concentration Variability in the Atlantic Water Inflow Region North of Svalbard. *J. Geophys. Res. Oceans* 126, e2020JC016522. <https://doi.org/10.1029/2020JC016522>
- Manley, T.O., Bourke, R.H., Hunkins, K.L., 1992. Near-surface circulation over the Yermak plateau in northern Fram Strait. *J. Mar. Syst.* 3, 107–125. [https://doi.org/10.1016/0924-7963\(92\)90033-5](https://doi.org/10.1016/0924-7963(92)90033-5)

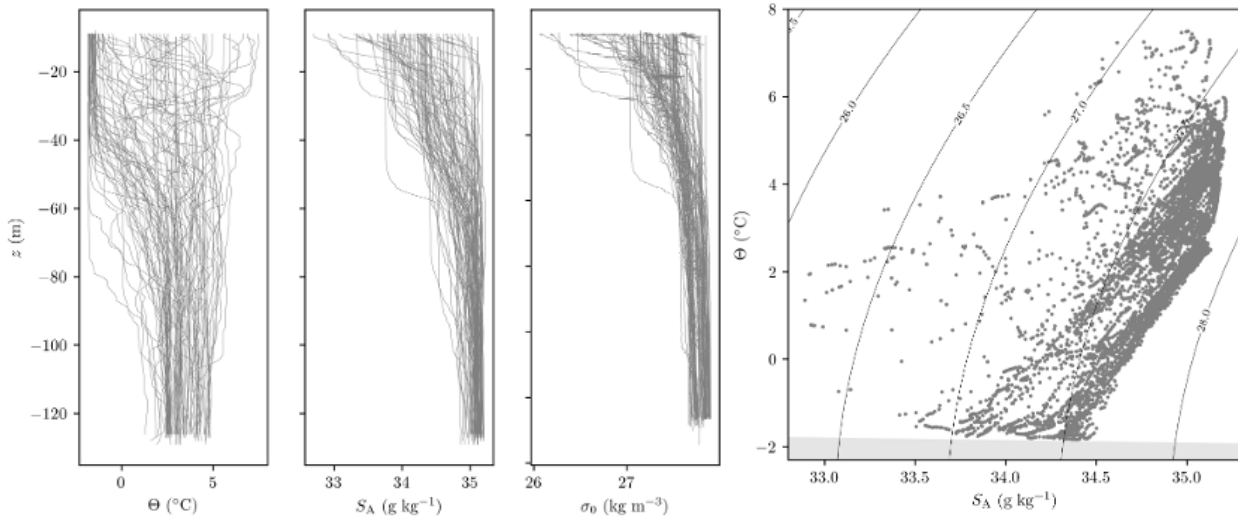
- Marnela, M., Rudels, B., Houssais, M.-N., Beszczynska-Möller, A., Eriksson, P.B., 2013. Recirculation in the Fram Strait and transports of water in and north of the Fram Strait derived from CTD data. *Ocean Sci.* 9, 499–519. <https://doi.org/10.5194/os-9-499-2013>
- Martin, T., Tsamados, M., Schroeder, D., Feltham, D.L., 2016. The impact of variable sea ice roughness on changes in Arctic Ocean surface stress: A model study. *J. Geophys. Res. Oceans* 121, 1931–1952. <https://doi.org/10.1002/2015JC011186>
- Matthes, L.C., Bélanger, S., Raulier, B., Babin, M., 2023. Impact of subsurface chlorophyll maxima on satellite-based Arctic spring primary production estimates. *Remote Sens. Environ.* 298, 113795. <https://doi.org/10.1016/j.rse.2023.113795>
- McPherson, R. A., von Appen, W-J., de Steur, L., Kanzow, T., Beszczynska-Möller, A., Renner, A., 'Decades of Change: Warming Trends and Variability of Atlantic Water as observed in the West Spitsbergen Current (1997–2024)'. Submitted to: Deep Sea Research Part II: LTR Hausgarten (under review).
- McPherson, R.A., Stevens, C.L., O'Callaghan, J.M., 2019. Turbulent Scales Observed in a River Plume Entering a Fjord. *J. Geophys. Res. Oceans* 124, 9190–9208. <https://doi.org/10.1029/2019JC015448>
- McPherson, R.A., Wekerle, C., Kanzow, T., 2023. Shifts of the Recirculation Pathways in Central Fram Strait Drive Atlantic Intermediate Water Variability on Northeast Greenland Shelf. *J. Geophys. Res. Oceans* 128, e2023JC019915. <https://doi.org/10.1029/2023JC019915>
- McPherson, R.A., Wekerle, C., Kanzow, T., Ionita, M., Heukamp, F.O., Zeising, O., Humbert, A., 2024. Atmospheric blocking slows ocean-driven melting of Greenland's largest glacier tongue. *Science* 385, 1360–1366. <https://doi.org/10.1126/science.ado5008>
- Menze, S., Ingvaldsen, R.B., Haugan, P., Fer, I., Sundfjord, A., Beszczynska-Möller, A., Falk-Petersen, S., 2019. Atlantic Water Pathways Along the North-Western Svalbard Shelf Mapped Using Vessel-Mounted Current Profilers. *J. Geophys. Res. Oceans* 124, 1699–1716. <https://doi.org/10.1029/2018JC014299>
- Mitchell, C., Drapeau, D., Pinkham, S., Balch, W.M., 2024. A chlorophyll *a*, non-photochemical fluorescence quenching correction method for autonomous underwater vehicles in shelf sea environments. *Limnol. Oceanogr. Methods* 22, 149–158. <https://doi.org/10.1002/lom3.10597>
- Morrison, A.T., Billings, J.D., Doherty, K.W., 2000. The McLane moored profiler: an autonomous platform for oceanographic measurements, in: OCEANS 2000 MTS/IEEE Conference and Exhibition. Conference Proceedings (Cat. No.00CH37158). Presented at the OCEANS 2000 MTS/IEEE Conference and Exhibition. Conference Proceedings, IEEE, Providence, RI, USA, pp. 353–358. <https://doi.org/10.1109/OCEANS.2000.881284>
- Muench, R.D., McPhee, M.G., Paulson, C.A., Morison, J.H., 1992. Winter oceanographic conditions in the Fram Strait-Yermak Plateau region. *J. Geophys. Res. Oceans* 97, 3469–3483. <https://doi.org/10.1029/91JC03107>
- Nicolaus, M., Katlein, C., Maslanik, J., Hendricks, S., 2012. Changes in Arctic sea ice result in increasing light transmittance and absorption. *Geophys. Res. Lett.* 39, 2012GL053738. <https://doi.org/10.1029/2012GL053738>
- Peralta-Ferriz, C., Woodgate, R.A., 2015. Seasonal and interannual variability of pan-Arctic surface mixed layer properties from 1979 to 2012 from hydrographic data, and the dominance of stratification for multiyear mixed layer depth shoaling. *Prog. Oceanogr.* 134, 19–53. <https://doi.org/10.1016/j.pocean.2014.12.005>
- Pérez-Hernández, M.D., Pickart, R.S., Torres, D.J., Bahr, F., Sundfjord, A., Ingvaldsen, R., Renner, A.H.H., Beszczynska-Möller, A., Von Appen, W., Pavlov, V., 2019. Structure, Transport, and Seasonality of the Atlantic Water Boundary Current North of Svalbard: Results From a Yearlong Mooring Array. *J. Geophys. Res. Oceans* 124, 1679–1698. <https://doi.org/10.1029/2018JC014759>
- Polyakov, I.V., Pnyushkov, A.V., Alkire, M.B., Ashik, I.M., Baumann, T.M., Carmack, E.C., Gosczko, I., Guthrie, J., Ivanov, V.V., Kanzow, T., Krishfield, R., Kwok, R., Sundfjord,

- A., Morison, J., Rember, R., Yulin, A., 2017. Greater role for Atlantic inflows on sea-ice loss in the Eurasian Basin of the Arctic Ocean. *Science* 356, 285–291. <https://doi.org/10.1126/science.aai8204>
- Prién, R.D., Schulz-Bull, D.E., 2016. Technical note: GODESS – a profiling mooring in the Gotland Basin. *Ocean Sci.* 12, 899–907. <https://doi.org/10.5194/os-12-899-2016>
- Quadfasel, D., Gascard, J.-C., Koltermann, K.-P., 1987. Large-scale oceanography in Fram Strait during the 1984 Marginal Ice Zone Experiment. *J. Geophys. Res.* 92, 6719. <https://doi.org/10.1029/jc092ic07p06719>
- Randelhoff, A., Fer, I., Sundfjord, A., 2017. Turbulent Upper-Ocean Mixing Affected by Meltwater Layers during Arctic Summer. *J. Phys. Oceanogr.* 47, 835–853. <https://doi.org/10.1175/jpo-d-16-0200.1>
- Rantanen, M., Karpechko, A.Yu., Lipponen, A., Nordling, K., Hyvärinen, O., Ruosteenoja, K., Vihma, T., Laaksonen, A., 2022. The Arctic has warmed nearly four times faster than the globe since 1979. *Commun. Earth Environ.* 3, 168. <https://doi.org/10.1038/s43247-022-00498-3>
- Reifenberg, S.F., Fer, I., Kanzow, T., Von Appen, W.-J., Hoppmann, M., Krumpen, T., Neudert, M., Preußner, A., Haas, C., 2025. Turbulence Observations below Drifting Sea Ice: TKE Production and Dissipation in the Meltwater-Influenced Boundary Layer. *J. Phys. Oceanogr.* 55, 451–470. <https://doi.org/10.1175/JPO-D-24-0102.1>
- Renner, A.H.H., Bailey, subsur, Reigstad, M., Sundfjord, A., Chierici, M., Jones, E.M., 2023. Hydrography, inorganic nutrients and chlorophyll a linked to sea ice cover in the Atlantic Water inflow region north of Svalbard. *Prog. Oceanogr.* 219, 103162. <https://doi.org/10.1016/j.pocean.2023.103162>
- Renner, A.H.H., Sundfjord, A., Janout, M.A., Ingvaldsen, R.B., Beszczynska-Möller, A., Pickart, R.S., Pérez-Hernández, M.D., 2018. Variability and Redistribution of Heat in the Atlantic Water Boundary Current North of Svalbard. *J. Geophys. Res. Oceans* 123, 6373–6391. <https://doi.org/10.1029/2018JC013814>
- Roemmich, D., Alford, M.H., Claustre, H., Johnson, K., King, B., Moum, J., Oke, P., Owens, W.B., Pouliquen, S., Purkey, S., Scanderbeg, M., Suga, T., Wijffels, S., Zilberman, N., Bakker, D., Baringer, M., Belbeoch, M., Bittig, H.C., Boss, E., Calil, P., Carse, F., Carval, T., Chai, F., Conchubhair, D.Ó., d'Ortenzio, F., Dall'Olmo, G., Desbruyeres, D., Fennel, K., Fer, I., Ferrari, R., Forget, G., Freeland, H., Fujiki, T., Gehlen, M., Greenan, B., Hallberg, R., Hibiya, T., Hosoda, S., Jayne, S., Jochum, M., Johnson, G.C., Kang, K., Kolodziejczyk, N., Kötzinger, A., Traon, P.-Y.L., Lenn, Y.-D., Maze, G., Mork, K.A., Morris, T., Nagai, T., Nash, J., Garabato, A.N., Olsen, A., Pattabhi, R.R., Prakash, S., Riser, S., Schmechtig, C., Schmid, C., Shroyer, E., Sterl, A., Sutton, P., Talley, L., Tanhua, T., Thierry, V., Thomalla, S., Toole, J., Troisi, A., Trull, T.W., Turton, J., Velez-Belchi, P.J., Walczowski, W., Wang, H., Wanninkhof, R., Waterhouse, A.F., Waterman, S., Watson, A., Wilson, C., Wong, A.P.S., Xu, J., Yasuda, I., 2019. On the Future of Argo: A Global, Full-Depth, Multi-Disciplinary Array. *Front. Mar. Sci.* 6, 439. <https://doi.org/10.3389/fmars.2019.00439>
- Roesler, C., Uitz, J., Claustre, H., Boss, E., Xing, X., Organelli, E., Briggs, N., Bricaud, A., Schmechtig, C., Poteau, A., D'Ortenzio, F., Ras, J., Drapeau, S., Haëntjens, N., Barbeau, M., 2017. Recommendations for obtaining unbiased chlorophyll estimates from in situ chlorophyll fluorometers: A global analysis of WET Labs ECO sensors. *Limnol. Oceanogr. Methods* 15, 572–585. <https://doi.org/10.1002/lom3.10185>
- Rudels, B., Björk, G., Nilsson, J., Winsor, P., Lake, I., Nohr, C., 2005. The interaction between waters from the Arctic Ocean and the Nordic Seas north of Fram Strait and along the East Greenland Current: results from the Arctic Ocean-02 Oden expedition. *J. Mar. Syst.* 55, 1–30. <https://doi.org/10.1016/j.jmarsys.2004.06.008>
- Salter, I., Bauerfeind, E., Fahl, K., Iversen, M.H., Lalande, C., Ramondenc, S., Von Appen, W.-J., Wekerle, C., Nöthig, E.-M., 2023. Interannual variability (2000–2013) of mesopelagic and bathypelagic particle fluxes in relation to variable sea ice cover in the eastern Fram Strait. *Front. Earth Sci.* 11, 1210213. <https://doi.org/10.3389/feart.2023.1210213>

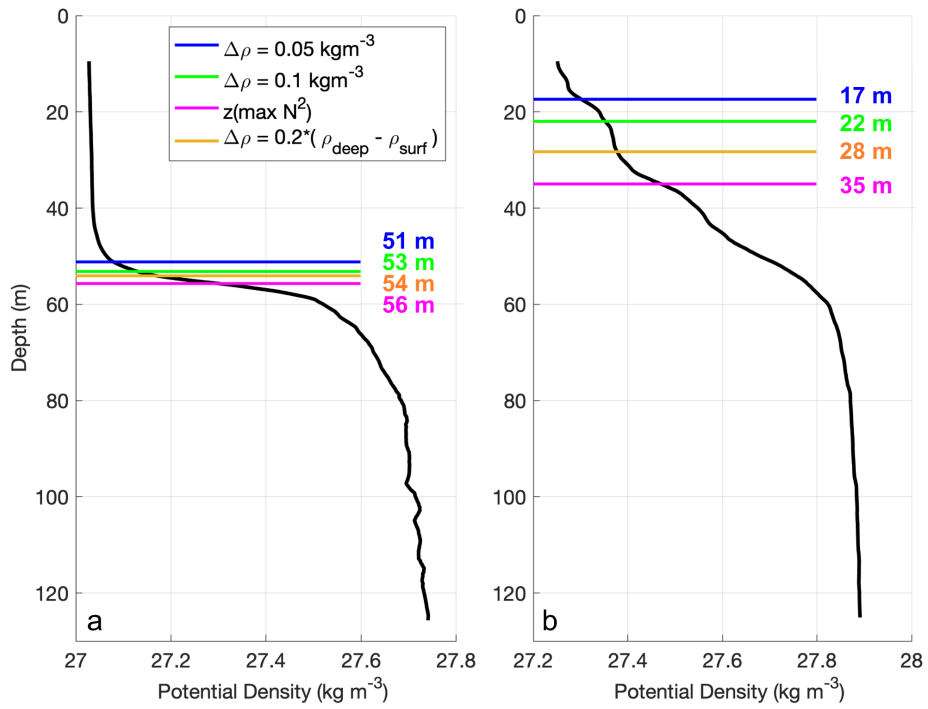
- Send, U., Fowler, G., Siddall, G., Beanlands, B., Pittman, M., Waldmann, C., Karstensen, J., Lampitt, R., 2013. SeaCycler: A Moored Open-Ocean Profiling System for the Upper Ocean in Extended Self-Contained Deployments. *J. Atmospheric Ocean. Technol.* 30, 1555–1565. <https://doi.org/10.1175/JTECH-D-11-00168.1>
- Shaw, W.J., Stanton, T.P., McPhee, M.G., Morison, J.H., Martinson, D.G., 2009. Role of the upper ocean in the energy budget of Arctic sea ice during SHEBA. *J. Geophys. Res. Oceans* 114, 2008JC004991. <https://doi.org/10.1029/2008JC004991>
- Skagseth, Ø., Orvik, K.A., Furevik, T., 2004. Coherent variability of the Norwegian Atlantic Slope Current derived from TOPEX/ERS altimeter data. *Geophys. Res. Lett.* 31, 2004GL020057. <https://doi.org/10.1029/2004GL020057>
- Smith, J.A., Pinkel, R., Goldin, M., Sun, O., Nguyen, S., Hughen, T., Bui, M., Aja, A., 2011. Wirewalker Dynamics. *J. Atmospheric Ocean. Technol.* 29, 103–115. <https://doi.org/10.1175/JTECH-D-11-00049.1>
- Soltwedel, T., Bauerfeind, E., Bergmann, M., Bracher, A., Budaeva, N., Busch, K., Cherkasheva, A., Fahl, K., Grzelak, K., Hasemann, C., Jacob, M., Kraft, A., Lalande, C., Metfies, K., Nöthig, E.-M., Meyer, K., Quéric, N.-V., Schewe, I., Włodarska-Kowalczuk, M., Klages, M., 2016. Natural variability or anthropogenically-induced variation? Insights from 15 years of multidisciplinary observations at the arctic marine LTER site HAUSGARTEN. *Ecol. Indic.* 65, 89–102. <https://doi.org/10.1016/j.ecolind.2015.10.001>
- Steele, M., Ermold, W., Zhang, J., 2011. Modeling the formation and fate of the near-surface temperature maximum in the Canadian Basin of the Arctic Ocean. *J. Geophys. Res. Oceans* 116, 2010JC006803. <https://doi.org/10.1029/2010JC006803>
- Stevens, C.L., Hill, P., Smith, M.J., Popinet, S., 2005. SUCA: An engine for repetitive autonomous profiling near the ocean surface. *Limnol. Oceanogr. Methods* 3, 300–307. <https://doi.org/10.4319/lom.2005.3.300>
- Strong, C., Rigor, I.G., 2013. Arctic marginal ice zone trending wider in summer and narrower in winter. *Geophys. Res. Lett.* 40, 4864–4868. <https://doi.org/10.1002/grl.50928>
- Timmermans, M.L., Marshall, J., 2020. Understanding Arctic Ocean Circulation: A Review of Ocean Dynamics in a Changing Climate. *J. Geophys. Res. Oceans* 125, 1–35. <https://doi.org/10.1029/2018JC014378>
- Timmermans, M.-L., Toole, J., Proshutinsky, A., Krishfield, R., Plueddemann, A., 2008. Eddies in the Canada Basin, Arctic Ocean, Observed from Ice-Tethered Profilers. *J. Phys. Oceanogr.* 38, 133–145. <https://doi.org/10.1175/2007JPO3782.1>
- Torres-Valdés, S., Tsubouchi, T., Bacon, S., Naveira-Garabato, A.C., Sanders, R., McLaughlin, F.A., Petrie, B., Kattner, G., Azetsu-Scott, K., Whitledge, T.E., 2013. Export of nutrients from the Arctic Ocean. *J. Geophys. Res. Oceans* 118, 1625–1644. <https://doi.org/10.1002/jgrc.20063>
- Villareal, T.A., Adornato, L., Wilson, C., Schoenbaechler, C.A., 2011. Summer blooms of diatom-diazotroph assemblages and surface chlorophyll in the North Pacific gyre: A disconnect. *J. Geophys. Res.* 116, C03001. <https://doi.org/10.1029/2010JC006268>
- Von Appen, W.-J., Baumann, T., Janout, M., Koldunov, N., Lenn, Y.-D., Pickart, R., Scott, R., Wang, Q., 2022. Eddies and the Distribution of Eddy Kinetic Energy in the Arctic Ocean. *Oceanography*. <https://doi.org/10.5670/oceanog.2022.122>
- von Appen, W.J., Waite, A.M., Bergmann, M., Bienhold, C., Boebel, O., Bracher, A., Cisewski, B., Hagemann, J., Hoppema, M., Iversen, M.H., Konrad, C., Krumpen, T., Lochthofen, N., Metfies, K., Niehoff, B., Nöthig, E.M., Purser, A., Salter, I., Schaber, M., Scholz, D., Soltwedel, T., Torres-Valdes, S., Wekerle, C., Wenzhöfer, F., Wietz, M., Boetius, A., 2021. Sea-ice derived meltwater stratification slows the biological carbon pump: results from continuous observations. *Nat. Commun.* 12. <https://doi.org/10.1038/s41467-021-26943-z>
- von Appen, W.-J., Wekerle, C., Hehemann, L., Schourup-Kristensen, V., Konrad, C., Iversen, M.H., 2018. Observations of a Submesoscale Cyclonic Filament in the Marginal Ice Zone. *Geophys. Res. Lett.* 45, 6141–6149. <https://doi.org/10.1029/2018GL077897>

Wang, X., Liu, Y., Key, J.R., Dworak, R., 2022. A New Perspective on Four Decades of Changes in Arctic Sea Ice from Satellite Observations. *Remote Sens.* 14, 1846. <https://doi.org/10.3390/rs14081846>

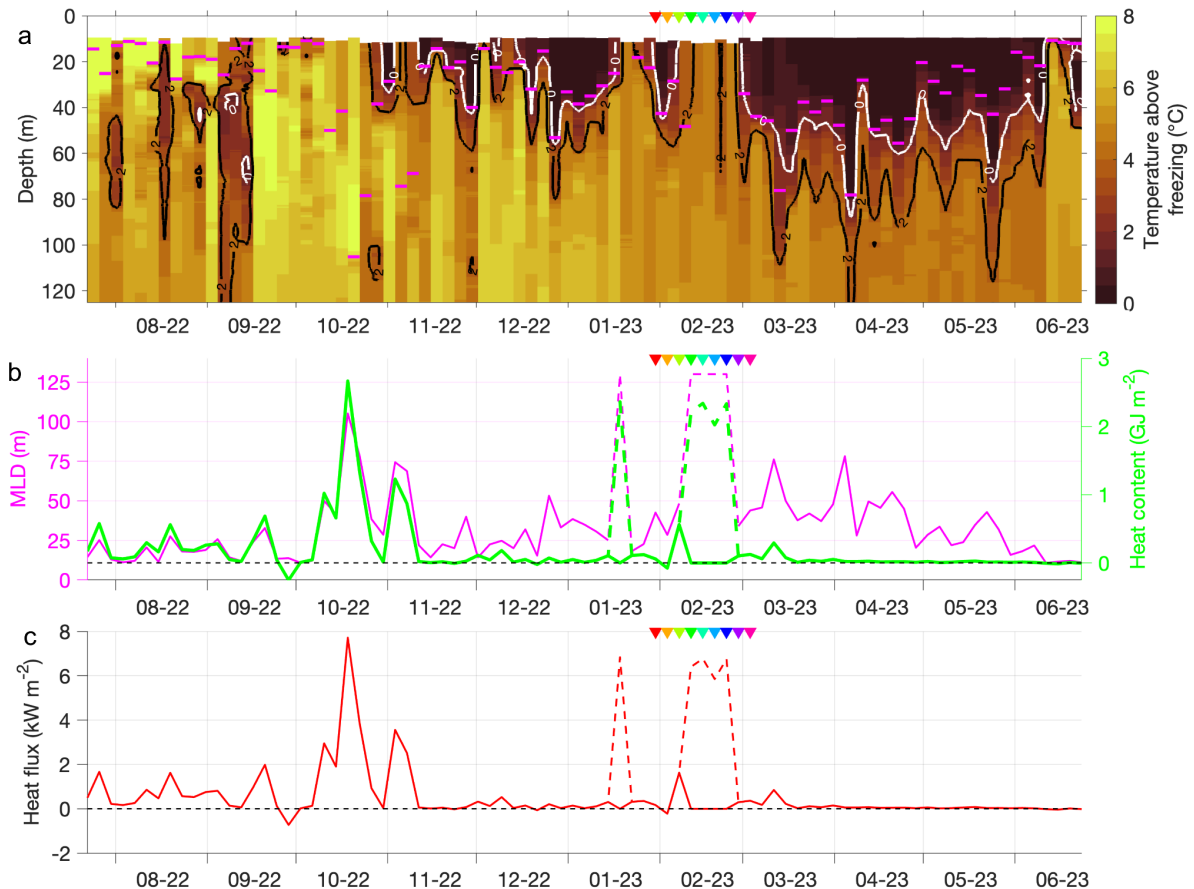
## Supplementary Figures



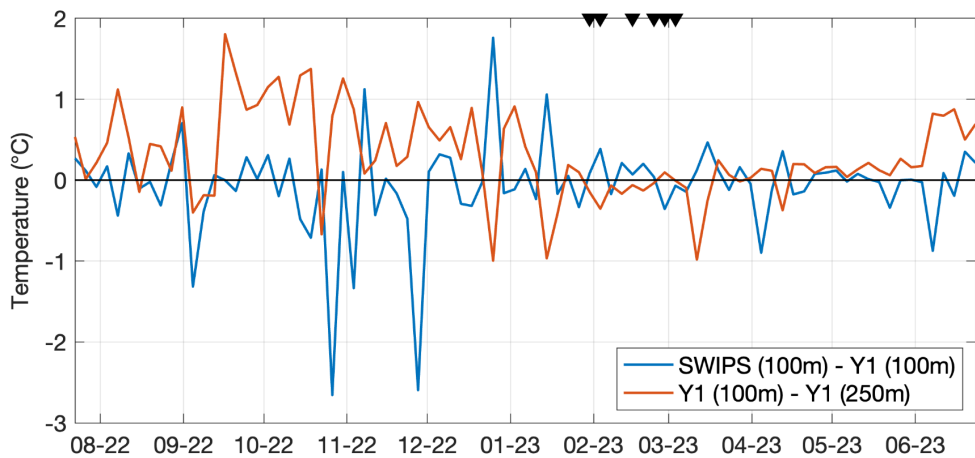
**Supplementary Figure 1:** Single profiles of (a) potential temperature, (b) absolute salinity, (c) density from the SWIPS profiler, and (d) the resulting T-S plot.



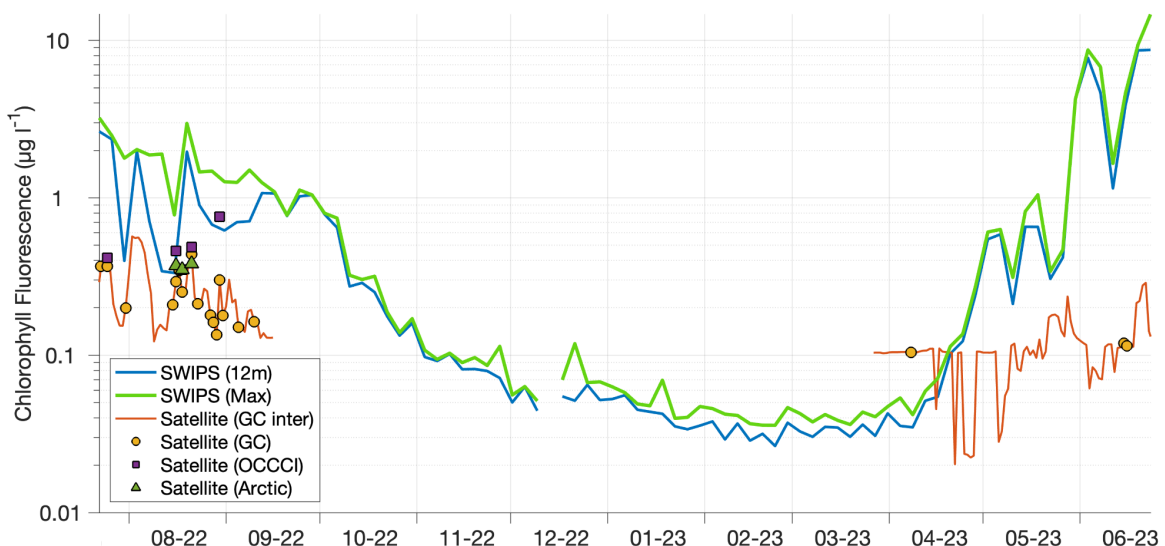
**Supplementary Figure 2:** Two selected potential density profiles from (a) December 2022 and (b) April 2023, illustrating estimates of mixed layer depth using the different methods described in Section 2.3.2.



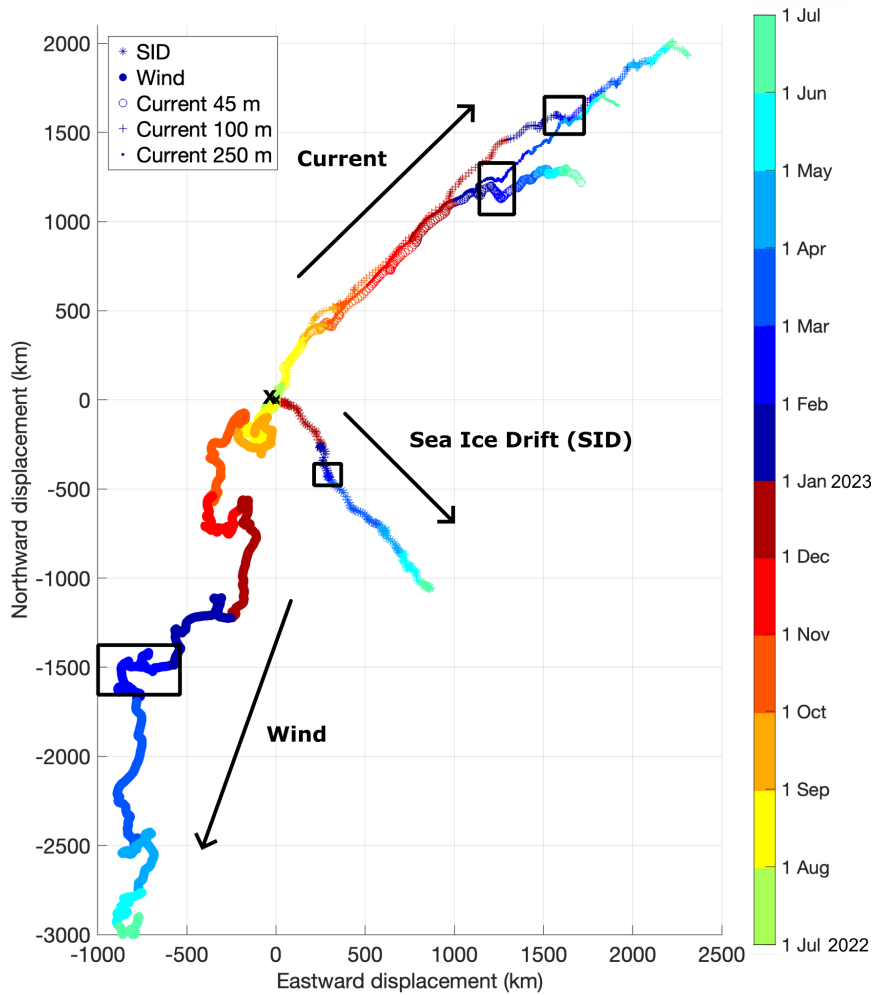
**Supplementary Figure 3: Ocean heat available in the mixed layer.** Timeseries of (a) temperature above freezing. The  $0^{\circ}\text{C}$  and  $2^{\circ}\text{C}$  isotherms are the labelled white and black contours respectively, and the mixed layer depth is the pink line. (b) Mixed layer depth (pink) and ocean heat content (green), and (c) ocean heat flux integrated over the depth of the mixed layer. The dashed lines in (b) and (c) assume the MLD is 130 m (i.e., deeper than the depth of the profiler). Here it is assumed that the difference in MLD-integrated heat content between consecutive profiles 4 days apart is solely explained by ocean-to-atmosphere heat flux. Positive heat flux is the potential for the ocean to release heat to the atmosphere. The chosen T-S profiles covering the AW event in Fig. 10 are the coloured triangles.



**Supplementary Figure 4:** Temperature difference at 100 m between SWIPS and Y1-1 (blue), and between 100m and 250 m at Y1-1 (orange). The chosen T-S profiles are the black triangles.



**Supplementary Figure 5: Comparison of near-surface chlorophyll products.** Timeseries of chlorophyll fluorescence at 12m (blue), maximum sub-surface chlorophyll (green) as measured by the SWIPS, and satellite-derived daily chlorophyll from three different products that covers the upper ~10m; Global Color (GC, circles); the gap-filled Global Color (orange line); OCCCI (squares) and specialist Arctic (triangles).



**Supplementary Figure 6: Trajectories over the Yermak Plateau.** Progressive vector diagram showing the integral advection of sea ice drift (SID), wind, and de-tided ocean velocities in the upper (45 m), mid (100 m) and deep (250 m) water column over the deployment period (July 2022 - June 2023). The deployment time (center) is marked by the black cross. The timing of the AW event in February 2023 and discussed in Section 4.1 is highlighted by the black boxes for each trajectory.